

Bioelectronic Screening Platform for Real-Time Monitoring of Tumour-derived Extracellular Vesicle-Induced Epithelial-to-Mesenchymal Transition

Walther Traberg

University of Cambridge

Johana Uribe

Cornell University

Victor Druet

King Abdullah University of Science and Technology (KAUST)

Adel Hama

KAUST

Chrysanthi-Maria Moysidou

University of Cambridge

Miriam Huerta

Cornell University

Reece McCoy

University of Cambridge

Daniel Hayward

University of Cambridge

Achilleas Savva

University of Cambridge

Amaury Genovese

University of Cambridge

Suraj Pavagada

University of Cambridge

Zixuan Lu

Imperial College London

Anil Koklu

KAUST

Anna-Maria Pappa

Khalifa University of Science and Technology

Rebecca Fitzgerald

University of Cambridge <https://orcid.org/0000-0002-3434-3568>

Sahika Inal

KAUST <https://orcid.org/0000-0002-1166-1512>

Susan Daniel

Cornell University

Roisin Owens (✉ rmo37@cam.ac.uk)

University of Cambridge <https://orcid.org/0000-0001-7856-2108>

Article

Keywords:

Posted Date: May 27th, 2022

DOI: <https://doi.org/10.21203/rs.3.rs-1697648/v1>

License: © ⓘ This work is licensed under a Creative Commons Attribution 4.0 International License.

[Read Full License](#)

Abstract

Tumour-derived extracellular vesicles (TEVs) induce the epithelial-to-mesenchymal (EMT) in non-malignant cells to promote invasion and cancer metastasis. As such, TEVs represent a novel therapeutic target in a field severely lacking in efficacious anti-metastasis treatments. However, scalable technologies that allow continuous, multiparametric monitoring of therapeutic response for identifying metastasis inhibitors are missing. Here, we report the development of a platform based on organic electrochemical transistors (OECTs) for the real-time monitoring of TEV-induced EMT and screening of anti-metastatic drugs. We used TEVs derived from the triple-negative breast cancer (TNBC) cell line MDA-MB-231, to induce EMT in non-malignant breast epithelial cells (MCF10A) over a 9-day period, recapitulating a model of invasive ductal carcinoma metastasis. We performed extensive biological validation using immunofluorescence (IF) imaging and protein expression analysis, providing mechanistic insight using an epigenetics approach, and demonstrate our ability to obtain multiparametric functional readouts of cells using OECTs. Further, by employing OECT-based phenotypic drug screening, we identify heparin as an effective blocker of TEV-induced EMT *in vitro*, showcasing a promising anti-metastatic drug.

Full Text

According to the WHO, cancer is a leading cause of death worldwide, accounting for nearly 10 million deaths, or one in six deaths in 2020 (<https://gco.iarc.fr/today>). The primary cause of cancer-related mortalities is widespread metastases, which are difficult to treat with therapeutic intervention^{12,13}. Meanwhile, drug development is a slow and costly process¹⁴, with a failure rate of 96.6% for FDA approvals in clinical trials for oncology¹⁵, primarily due to insufficient efficacy (48%/55%) or safety (25%/14%; phase II/III)¹⁶. Therefore, the development of better pre-clinical drug screening technologies and disease models is a healthcare imperative. Although metastasis is a hallmark of cancer, it remains poorly understood^{12,17}, in part due to challenges in characterising the spatial and temporal progression of this malignancy¹⁷. Recently, nano-sized particles secreted by tumour cells implicated in intercellular communication, called extracellular vesicles (EVs), have been found to play a pivotal role in metastasis^{18,19}. Tumour-derived (T)EVs carry functional oncogenic biomolecules that confer oncogenic potential²⁰ and induce malignant transformation²¹ in recipient cells to drive a process called the epithelial-to-mesenchymal transition (EMT)¹⁹; a central component of metastasis. EMT is a reversible process by which epithelial cells at the invasive front of carcinoma acquire a mesenchymal phenotype²² and develop the ability to migrate, invade²³, and disseminate via circulation to form metastases in distal organs¹. Targeting TEVs with therapeutic intervention could represent a novel avenue for preventing EMT, and thereby metastasis occurrence¹⁹. However, current sensing technologies and phenotypic screening assays suffer from inherent trade-offs between the density of information gained and the ability to study a complex biological/cellular system in its native state, which is particularly detrimental to the study of transient biological processes, such as EMT. This hampers the discovery of new pharmacological

strategies targeting TEV dysregulation pathways that could aid the development of antimetastatic drugs²⁴.

Phenotypic drug discovery approaches incorporating cell-based disease models have the potential to address the incompletely understood complexity of diseases, compared to target-based drug discovery. Although phenotypic screening can be an attractive proposition for efficiently identifying functionally active hits that lead to first-in-class drugs²⁵, current readouts rely on sensing technologies that are invasive; perturbing the system of study (e.g. omics), produce discrete data, and/or scale poorly (e.g. microscopy imaging)^{26,27}. This makes it difficult to investigate the temporal relationship between measured pharmacodynamic response and pharmacokinetics for quantitative translation to *in vivo* outcomes²⁸. Moreover, utilising low-throughput technologies to screen thousands of potential hits during the early stages of drug discovery is cost- and time-prohibitive²⁹. Thus, there is a pressing need to integrate disease-relevant cell-based models with novel, scalable sensing technologies that produce unbiased high-content and multiparametric readouts, ideally in a continuous manner, without disrupting the native state of the system of study²⁵. Here, we present a platform based on organic bioelectronic technology that fulfils these requirements.

The field of organic electronics has progressed enormously since the initial discovery of conducting polymers³⁰ and has recently gained widespread applications in biomedical research. The physiochemical properties of organic electronic materials, often establishing a direct conduit between biological and electrical signals, have enabled the development of novel (bioelectronic) tools/devices to transduce biological signals with the outmost sensitivity. One example is the organic electrochemical transistor (OECT), a device that has been integrated with *in vitro* models of varying complexity spanning from plasma membranes to 3D complex cell cultures^{31–37}. OECTs are ideally suited for biological interfacing on the one hand due to their inherent at-source signal amplification properties³⁸ and on the other hand due to their biocompatibility, comprising of polymer-based materials^{38,39}. OECTs adopt a transistor three-terminal configuration consisting of source and drain, on either side of a conducting polymer channel, and one gate electrode that controls the channel conductivity. Belonging to the broader class of “electrolyte gated transistors”, OECTs operate in direct contact with an electrolyte⁴⁰ and their operation relies on ions being “pushed” into the conducting polymer channel upon application of a gate bias, changing its doping state, hence its conductivity⁴¹. The coupling between ionic (from the gate electrode) and electronic (from the drain electrode) charges within the entire volume of the conducting polymer channel is a particularly interesting feature of this device configuration with record high signal amplification values that scale with the volume of the channel⁴². Hence, OECTs, have been widely considered as especially promising biological signal amplifiers^{43,44} without necessitating the incorporation of external circuits. The conducting polymer poly(3,4-ethylenedioxythiophene) doped with poly(styrene sulfonate) (PEDOT:PSS) has been by and large the material of choice in OECTs due to its excellent stability and easy processability⁴⁵. When in contact with aqueous biological environments, PEDOT:PSS swells, providing a biocompatible hydrogel-like interface for cells⁴⁶, and exhibiting a large

volumetric capacitance⁴⁷. Another key feature of PEDOT:PSS is its optical transparency (when deposited as a thin film), making it compatible with microscopy, thereby enabling simultaneous optical and electrical readouts^{31,34,35}, pivotal in biological assays. PEDOT:PSS-based OECTs have been used to monitor cell coverage and differentiation, as well as epithelial barrier integrity both in Transwell format and with cells adhered directly on the device surface^{31,33,48,49}. The latter involves the growth of a monolayer of cells on the channel and the gate, which introduces a barrier for ion motion in the electrolyte (cell culture media), directly affecting the transistor output and in effect using the OECT as an impedance biosensor^{33,50}. Monitoring tight junction modulation, nephrotoxicity, cancer invasion, wound-healing, and toxicology^{32,33,51–53} are only some of the various application areas where impedance-based OECTs interfaced with cell cultures have been successfully used, although biological validation of the electrical readouts has been limited in scope to date.

Capitalising on its key attributes, interfacing OECTs with a cell-based EMT-disease model could address current issues facing sensing technologies and unlock higher throughput phenotypic screening for drug discovery. We propose utilising OECTs and electrical measurements to continuously monitor EMT *in vitro* and to produce high-content, quantitative, time-series data that can be correlated with cell phenotype. We integrated OECTs with MCF10A cells; a normal, non-tumorigenic, pre-neoplastic mammary cell line^{54,55}, and exposed these to TEVs derived from MDA-MB-231 cells; a highly aggressive and invasive triple-negative breast cancer (TNBC) cell line⁵⁶, to recapitulate a model of invasive ductal carcinoma (**Fig. 1, Supplementary Discussion 1**). Key features of this work are: (1) isolating and characterising EVs; (2) investigating the ability of TEVs to induce EMT in MCF10A cells using combined electrical and biological readouts, providing mechanistic insight using an epigenetics approach; and (3) developing a robust and scalable platform for the functional screening of anti-cancer/antimetastatic drugs, e.g. heparin.

Here, we demonstrate the ability of the OECT to monitor TEV-induced EMT in real-time, without compromising compatibility with conventional end-point assays. We leverage the capabilities of OECT devices to provide a continuous, label-free, non-disruptive, and *quantitative* measure of EMT *in vitro*, using electrical measurements as a novel functional readout of a metastatic process, as well as of TEV function. We validate the electrical readouts with molecular biology and optical microscopy techniques to validate the OECT-based measurements. Finally, we demonstrate that we can dynamically monitor therapeutic response and find that heparin, a competitive inhibitor of cell surface receptors, effectively abrogates TEV-induced EMT in MCF10A cells, showcasing the drug screening capabilities of the platform.

Results And Discussion

Characterisation of extracellular vesicles. In the present study, MCF10A cells were exposed to either MDA-TEVs or EVs derived from non-tumorigenic human embryonic kidney (HEK)293 cells (HEK-EVs), to demonstrate that the associated EMT-inducing effect was caused by TEVs specifically, rather than EVs in general – a so-called specificity check. EVs were isolated by ultracentrifugation, but without further

purification to avoid compromising particle yield and may therefore be described as crude EVs. EVs were characterised following the guidelines of The International Society for Extracellular Vesicle (ISEV) for EV research⁵⁷, which include EV quantification by particle number and total protein content, protein markers expected and not expected to be present in enriched EV samples, and single vesicle analysis. Samples were enriched in the classic EV protein biomarkers CD9 and CD63. Samples did not contain calreticulin; a protein located in the endoplasmic reticulum, nor annexin A1; a microvesicle (150-1,000 nm sized EVs) biomarker⁵⁸ (**Fig. 2a**), as expected. Nanoparticle tracking analysis (NTA) revealed heterogenous EV populations, with peak particle sizes of 153 ± 5.1 nm and 112 ± 12.7 nm for MDA-TEVs and HEK-EVs, respectively (**Fig. 2b**). Although such EVs may qualify as exosomes, without confirmation of their endosomal origin, they should be characterised as CD63-positive EVs⁵⁷. Interestingly, EV particle concentration varied by a factor of >6 between the cell types, with $145 \times 10^9 \pm 2.3 \times 10^9$ MDA-TEVs and $22.7 \times 10^9 \pm 0.8 \times 10^9$ HEK-EVs derived from the same number of cells. This is consistent with reports that cancer cells produce an overabundance of EVs compared to healthy cells^{59,60}, with their biogenesis possibly enhanced by hypoxic conditions prevalent in the tumour microenvironment (TME)⁶¹. This difference was equally reflected in the total protein amount, (**Table 1**). EVs had particle zeta potentials of -12.6 ± 0.62 mV for MDA-TEVs and -6.2 ± 0.25 mV for HEK-EVs, as expected⁶². EVs displayed characteristic spherical and cup-shaped morphologies on TEM micrographs, and size heterogeneity is apparent with vesicles ranging from 50-200 nm in diameter (**Fig. 2c**). Immunogold labelling of MDA-TEVs was performed to confirm the presence of CD63 on the EV's surface (**Fig. 2cii**).

EV	Size (nm)	ζ-potential s(mV)	Concentration (billion particles/ml)	Protein content (µg/ml)	Ratio of µg protein to billion particles
MDA-TEV	153 ± 5.1	-12.6 ± 0.62	145 ± 2.3	2411 ± 23.2	16.6
HEK-EV	112 ± 12.7	-6.2 ± 0.25	22.7 ± 0.8	350 ± 3.5	15.4

Table 1: EV characterisation data. Mean ± s.e.m.; values calculated from measurements of EVs collected from n=2 and 3 different cell passages for each cell line for NTA/zeta potential and protein concentration, measured using a Qubit 4 fluorometer, respectively.

Continuous OECT-based monitoring of TEV-induced EMT. Current cell-based approaches and accompanying sensing technologies suffer from limitations that result in the loss of useful information and hamper the development of therapeutic interventions against EMT. End-point assays that yield discrete data require multiple time-points to be incorporated into the experimental design to track the dynamic changes that occur during EMT. While functional assays, such as migration or invasion assays, allow functional changes to be assessed, these are often limited to optical techniques, which are

inherently low-throughout and semi-quantitative at best. To address this, we developed a novel functional readout of EMT using dynamic impedance-based monitoring on OECTs to probe changes in epithelial cell barrier integrity resulting from malignant transformation. The electrical “tightness” of a cellular monolayer reflects the ionic conductance of the paracellular and transcellular pathways in an epithelial monolayer⁶⁴. Although strictly speaking this should be measured on a Transwell format, the resistance of cells adhered on substrates has previously been measured and correlates with barrier cell differentiation to epithelial phenotypes⁴⁸. Resistance of the cell layer is a quantitative measure of barrier integrity and permeability, and, as such, can be correlated to the EMT status of cells (**Fig. 1**). We postulated that the ability to continuously and non-invasively monitor cell phenotype during EMT could help shed light on the incidence and implication of EMT hybrid states in metastasis and elucidate the timescales of TEV function; a crucial insight for developing potent therapeutic interventions (see **Supplementary Discussion 2**).

To achieve this, we had to adapt our OECT platform to ensure that it was compatible with long-term monitoring studies and could be integrated seamlessly with the EMT-model. Previous studies had functionalised the OECT surface with collagen type I to promote cell adhesion^{32,52}. However, collagen type I promotes EMT and tumour invasion in cancer cells^{65,66}. Therefore, to avoid any confounding variables, we forewent any surface functionalisation and instead incubated the OECTs with normal MCF10A culture media overnight prior to cell seeding to promote adherence of cells. Moreover, the commonly used external Ag/AgCl electrodes^{52,53} are cytotoxic^{67–69} and thus inappropriate for long-term studies. Instead, we opted to use a planar Au gate electrode to ensure that the devices produced stable outputs over extended periods of time. The absence of any external electrode also reduced the risk of contamination considerably and improved data acquisition times.

The addition of an insulating cell layer between the channel (**Fig. 3a**) and the gate affects the OECT gating efficiency, rendering the device slower to respond to a given applied gate bias³⁵. The modulation of the device response time serves as a measure of the epithelial barrier integrity and is defined as the cut-off frequency, which corresponds to the frequency at 70.7% of the maximum transconductance⁴⁸. The cut-off frequency is a figure of merit that defines the regimes of high and low ionic transport⁴³. Another important readout relevant to cells undergoing EMT can be derived from impedance measurements of the OECT channel as a function of frequency. As shown in the inset of **Figure 3b**, the impedance of the channels increases for frequencies over ~2KHz. At this frequency range, the impedance of our system is dominated by the resistance of the cell layer with the effect of capacitance being negligible⁷⁰. Therefore, we can directly correlate this increase of impedance with the cell layer resistance.

To assess the ability of MDA-TEVs to promote EMT in MCF10A cells, four experimental conditions were tested: (1) non-treated cells cultured with normal medium; (2) cells treated with MDA-TEVs representing the treatment condition; (3) cells treated with transforming growth factor beta 1 (TGF- β 1) representing a positive control, as TGF- β 1 is commonly used to induce EMT in epithelial cells^{71–73}; and (4) cells treated with HEK-EVs representing a negative control and a specificity check. The culture medium (normal or

supplemented with MDA-TEVs, HEK-EVs, or TGF- β 1) was refreshed every 48 hours, thereby exposing the cells to fresh EVs or TGF- β 1 every two days (see **Schematic S1**). Throughout the experimental period, the activity of cells growing on the devices was monitored via daily OECT measurements. **Figure 3a** (see also **Fig. S2**) illustrates highly viable cells on the devices at the end of the experimental period, assessed by cytotoxicity/viability assays (LIVE/DEAD), assay) revealing an exceedingly high ratio of live-to-dead cells. This also highlights the added benefit of using the OECT which has a transparent channel that can be used to image the cells.

Cells present on the transistor channel and the gate electrode induce a shift in the cut-off frequency (**Fig. 3c**), which decreases as the cells continue to grow and differentiate, creating a barrier to the ion flux and slowing the response of the device. This is equally reflected in the extracted cell layer resistance (R_{cl}) data, which increases over time (**Fig. 3c, Fig. S3**). The cut-off frequency was normalised to treatment day 0 for each condition (**Fig. 3d**), as the treatments were started at this time and to account for device-to-device performance variation.

A two-way ANOVA was performed to analyse the effect of treatment condition and treatment time on cut-off frequency. Within conditions, a two-way ANOVA showed that there was not a statistically significant difference in mean normalised cut-off frequency between day 0 and day 9 for non-treated cells ($F(1,45)=54.88$, $p=.92$) with $M_{diff}=0.17$ (-17%) and cells treated with HEK-EVs ($F(1,45)=54.88$, $p=.86$) with $M_{diff}=0.20$ (-20%). A small decrease in normalised cut-off frequency is observed in both conditions, which may be caused by the tightening of the lateral cell-cell junctions, as cells continue to differentiate and form an insulating barrier on the device. An asymptotic regression analysis revealed that the normalised cut-off frequency of non-treated MCF10A cells tends towards 0.88 \pm 0.034 (**Fig. S4a**). There was, however, a statistically significant difference in mean normalised cut-off frequency between day 0 and day 9 for cells treated with MDA-TEVs ($F(1,45)=54.88$, $p<.000$) with $M_{diff}=1.24$ (+124%) and cells treated with TGF- β 1 ($F(1,45)=54.88$, $p<.000$) with $M_{diff}=1.09$ (+109%). This increase in cut-off frequency indicates an increase in the “leakiness” of the cell monolayer. This is in line with the degradation of cell-cell junctions⁷⁴, characteristic of cells undergoing EMT, leading to an increase in paracellular ion flux into the PEDOT:PSS channel⁷⁵. Optical imaging illustrates that cells are present and alive on the channel (**Fig. 3a, 4b**), although the changes in paracellular ion flux are not visible, in contrast to the highly sensitive OECT-based measurements of changes in paracellular flux caused by EMT, enabling real-time monitoring of cell phenotype transition. Interestingly, it appears that MDA-TEVs initially promote degradation of epithelial barrier integrity faster than TGF- β 1, during treatment day 0 to 4, after which point the effect of both treatments are comparable. This is in line with previously reported timescales of TEV and TGF- β 1-induced EMT^{72,76,77}.

Additionally, mean normalised cut-off frequency was compared between treatment conditions on day 9 (**Fig. 3e**). A two-way ANOVA showed that there was a statistically significant difference in mean normalised cut-off frequency on day 9 between non-treated cells and cells treated with either MDA-TEVs ($F(3,45)=35.20$, $p<.000$) with $M_{diff}=1.41$ (171%) or TGF- β 1 ($F(3,45)=35.20$, $p<.000$) with $M_{diff}=1.27$ (153%).

Whereas there was not a statistically significant difference in mean normalised cut-off frequency on day 9 between non-treated cells and cells treated with HEK-EVs ($F(3,45)=35.20$, $p=1.$) with $M_{diff}=0.021$ (-3%). This demonstrates our ability to compare different treatment conditions conducted on different OECT devices to one another, which holds promise for scaled-up operation and confirms that the observed effect is caused by the intervention (MDA-TEV or TGF- β 1). Lastly, a simple linear regression was used to test if MDA-TEV treatment time significantly predicted the mean normalised cut-off frequency (**Fig. S5**). The fitted regression model was:

$$\text{Normalised cut-off frequency} = 1 + 0.134 (\pm 0.008) \times \text{MDA-TEV treatment time} \quad (1)$$

The overall regression was statistically significant ($R^2=.978$, $F(1,69)=1527.60$, $p<.000$) and it was found that MDA-TEV treatment time significantly predicted mean normalised cut-off frequency ($\beta=0.134$, $p<.000$). This indicates that the kinetics of the degradation of epithelial barrier integrity in this regime (0-9 days of MDA-TEV treatment) can be represented by a linear approximation. We would assume that the linear regime only represents a slice of the epithelial barrier degradation process, as the cells progress through EMT. The overall kinetics could potentially be represented by a logistic regression model (with its characteristic S-shape) with a maximum corresponding to the cut-off frequency when no cells are present in the channel. As cell barrier integrity invariably is associated with cell phenotype⁴⁸ and by extension EMT status^{12,74}, our platform is thus able to provide insight into the kinetics governing TEV-mediated EMT. This is highly applicable to predicting therapeutic response and modelling the relationship between TEV/drug treatment dose/time and epithelial barrier integrity.

Compared to previous studies, which assessed the effects of MDA-TEVs up to 48 hours post treatment^{76,77}, we demonstrate continuous monitoring of MDA-TEV-induced EMT over a 9 day period and elucidate/establish a linear relationship between MDA-TEV treatment time and epithelial barrier integrity/EMT status. The ability to continuously monitor a transient process in a dynamic system is ideal for assessing drug response over time. To validate the electrical readouts, biomolecular assays were carried out to assess the change in cell phenotype and determine EMT.

Biological validation of OECT measurements by immunofluorescence and immunoblots. In our study, to validate the electrical readouts and establish cut-off frequency and impedance as a credible figure of merit for EMT, we determined cell phenotype and defined EMT status by analysis and quantification of gene expression of classic EMT markers using immunoblots and ELISA. Additionally, we performed IF confocal imaging to assess protein expression and location profiles and measure cell height and morphology. IF confocal imaging was performed both on samples fixed 48 hours after treatment, as previous studies report TEV-induced changes within this timeframe^{76,77}, and on samples fixed on OECTs treatment day 9. An N-cadherin based ELISA was performed on treatment day 7 and whole-cell lysates were collected on treatment day 9 for immunoblot analysis.

After 48 hours of exposure to MDA-TEVs or TGF- β 1, vimentin expression markedly increased in the treated cells and remodelling of F-actin is apparent with the appearance of actin stress fibres inside the

cells, as opposed to the cortical thin actin bundles in the non-treated cells (**Fig. 4a**, see **supplementary discussion 3**). After 9 days of treatment, F-actin stress fibres are still present (**Fig. 4b**). Additional confocal IF images of MCF10A cells stained for E-cadherin, N-cadherin, and nuclei are available in **Fig. S6**. Cell density, as measured by the number of nuclei per area, decreased by 23% and 44% with MDA-TEV and TGF- β 1 treatment, respectively (**Fig. 4c**). This is caused by individual cells occupying a larger area, which indicates a flattening of the cells, consistent with the transformation from the apical-basal polarity of epithelial cells to the back-front polarity of migratory mesenchymal cells⁷⁴. The accompanying functional changes to the cells was captured by the OECT measurements, as cut-off frequency increased in the same 48-hour period (**Fig. 4d**), indicating that changes to lateral cell-cell adhesion have already begun and is readily detectable by the OECT. This holds promise for the utilisation of the OECT platform to provide better temporal resolution of TEV-induced EMT.

To further substantiate these findings, confocal microscopy was employed to evaluate the height of cells hosted on the OECT channel, as changes in cell height can be used to imply phenotypic switching during EMT⁷⁹. Z-stacked confocal images of cells in the OECT channel, labelled for F-actin and nuclei, were obtained on day 9 of the experimental period (**Fig. 4b**, **Fig. S7**, **Supplementary Videos 1-3**). Cell height varied between non-treated and treated cells, mirroring the trend of cell layer resistance derived by OECT monitoring (**Fig. 4e**), and clearly demonstrating the unique ability of our platform to directly correlate a biological event with a corresponding electrical readout, both occurring in the channel. To assess the degradation of cell-cell junctions and define EMT, the samples were probed for several hallmark EMT proteins. Treated cells had increased expression of vimentin, N-cadherin, and fibronectin, (mesenchymal markers) and decreased expression of E-cadherin (epithelial marker), while F-actin expression remain constant (**Fig. 4f-h**). This evidences the occurrence of the cadherin switch (from E- to N-cadherin) and corroborates vimentin upregulation as seen on confocal images (**Fig. 4a**). ELISA-based N-cadherin protein expression revealed that N-cadherin on treatment day 7 in the MDA-TEV- and TGF- β 1-treated cells was 19- and 15-fold higher, respectively, compared to the non-treated cells (**Fig. 4f**). Cells treated with HEK-EVs did not exhibit differential expression of these markers compared to non-treated cells (**Fig. 4g-h**), indicating that it is specifically MDA-TEVs that mediate EMT.

Our biological validation data strongly indicate that MDA-TEV treatment promotes EMT in MCF10A cells. Additionally, we demonstrate the multiplexing capability of the OECT platform by correlating the height of cells in the transistor channel to the cell layer resistance, R_{cell} , measured in the same channel. This ability to directly correlate an electrical signal with a biological readout is highly beneficial for furthering our understanding of EMT.

MDA-TEVs do not influence TWIST1 and TFPI2 DNA methylation levels. Next, we sought to gain mechanistic insight into MDA-TEV-induced EMT via epigenetics analysis. Epigenetic remodelling is prevalent during breast cancer metastasis⁸⁰ and DNA methylation of tumour and metastasis suppressor genes is a hallmark of circulating tumour cells⁸¹. Gene promoters, especially key tumour suppressor genes, are unmethylated in normal tissues and highly methylated in cancer tissues⁸². In this way, gene

promoter hypermethylation is a pathway for repression of gene transcription (transcriptional silencing), and conversely, gene promoter hypomethylation (loss of DNA methylation) may promote gene expression⁸³. Oncogene BCR-ABL1-positive EVs released from leukaemia cells have been demonstrated to increase global DNA methylation levels in recipient cells⁸⁴. With this in mind, we sought to determine whether MDA-TEVs influence DNA methylation by analysing the methylation status of the tumour suppressor gene tissue factor pathway inhibitor 2 (TFPI2) and the pro-metastatic transcription factor TWIST1. TWIST1 represses E-cadherin and promotes EMT⁷⁶ and is negatively associated with TFPI2 in breast cancer patients, as TFPI2 suppresses breast cancer progression through inhibiting TWIST-integrin $\alpha 5$ pathway⁸⁵. TFPI2 is downregulated in breast cancer cells lines compared to MCF10A cells and methylation in the TFPI2 promotor has been found in highly invasive breast cancer cells⁸⁶. TWIST1 transcripts were reportedly upregulated after MDA-TEV treatment^{76,77} (Fig. 5a) and we observed a down-regulation of E-cadherin between treatment and non-treatment conditions (**Fig. 4g-h**), indicating E-cadherin repression. However, MDA-TEVs do not appear to carry TWIST1 (Fig. 5b)

A MethyLight-based approach was used to determine the methylation of these markers⁸⁷. This was based on previous work published by Chettouh et al (2018), which looked at markers of Barrett's oesophagus for methylation⁸⁸. We found that neither TFPI2 nor TWIST1 was significantly differentially methylated between non-treated and MDA-TEV-treated cells (**Fig. 5c**). Surprisingly, TFPI2 displayed higher levels of methylation compared to TWIST1 across both conditions. This raises the question of whether TFPI2 (and TWIST1) methylation status in MCF10A cells could potentially contribute to the cell line's intrinsic phenotypic plasticity for mesenchymal transition.

Interesting, immunoblot analysis revealed that TWIST1 protein was differentially expressed between the two conditions (**Fig. 5a, d**), which could suggest that TWIST1 protein expression is being repressed post-transcriptionally in non-treated MCF10A cells, e.g. by CPEB1/2 and miR-580⁸⁹. miR-580 acts as a negative regulator of TWIST1 expression in MCF10A cells and is downregulated in MCF10A cells which have undergone EMT⁸⁹. As cells treated with MDA-TEVs exhibit relatively higher levels of TWIST1, TWIST1 protein expression could be upregulated post-transcriptionally by other regulatory mechanisms, e.g. MDA-TEV-delivered miR-580-silencing circular RNAs⁹⁰, or even be induced by upregulation of transcriptional factors, e.g. HMGA2⁹¹. Further immunoblot analysis revealed that TWIST1 was not part of MDA-TEV cargo, although highly expressed in MDA-MB-231 cells (**Fig. 5b**). These results collectively indicate that MDA-TEVs are dysregulating endogenous TWIST1-repression in MCF10A cells via mechanisms other than epigenetic remodelling or direct protein transfer.

Heparin treatment blocks TEV-induced EMT. Given that EMT determines the most lethal feature of cancer, metastasis, it represents an attractive target in oncology. However, direct targeting of EMT effector molecules is, in most cases, pharmacologically challenging⁹². Previous anti-EMT strategies have targeted signalling pathways, molecular drivers, or the mesenchymal cells themselves⁹³, and several clinical trials targeting EMT are ongoing⁹⁴. Recent efforts using nitrofen and its analogues to interfere with the process of EMT have proven efficacious in blocking TNBC metastasis and invasiveness both *in vivo* and *in*

*vitro*⁹⁵. Such reports underscore the importance of identifying pharmacological targets against EMT to prevent metastasis. Moreover, as EMT increases drug resistance⁹⁶, targeting EMT could also attenuate cancer cell stemness and increase the effectiveness of more classic chemotherapeutic⁹⁷. There is therefore an imminent need to elucidate the role of TEVs in EMT to identify new anti-cancer strategies that target TEVs.

We selected heparin as a possible TEV-targeting, anti-EMT treatment and leveraged our platform to screen this candidate drug. Heparin is a glycosaminoglycan commonly used as an anticoagulant drug. However, it is reported to have anti-cancer effects in humans^{98–101} and has been shown to decrease metastasis in animal models¹⁰². The mechanism for heparin's anti-metastatic effect has been proposed to be a blocking function in tumour cell/platelet interactions^{103,104}. In addition to this mechanism, heparin's anti-cancer role may involve regulating TEV uptake into recipient cells¹⁰⁵. EVs depend on cell-surface heparan sulfate proteoglycans (HSPGs) for their internalisation and functional activity and heparin is a competitive inhibitor of cell surface receptors dependent on HSPG coreceptors^{7,105,106}. Heparin treatment of cells and/or EVs is known to interfere with TEV binding to the cell surface^{7,105,106} (**Fig. 6a**), and heparin has been reported to partially block EV-transfer of EGFRvIII mRNA into recipient cells¹⁰⁵ and significantly reduce EV-mediated stimulation of cancer cell migration and invasion^{4,7}. This function makes HSPGs a potential target for inhibition of TEV-mediated tumour development and proliferation. To test the efficacy of heparin in preventing MDA-TEV-induced EMT, a two-factor factorial experiment was designed, where cells were incubated with or without MDA-TEVs in the presence or absence of heparin (**Fig. 6b**).

Heparin treatment of cells effectively ablated the EMT-promoting effect of MDA-TEVs and heparin itself does not appear to adversely affect the barrier forming properties of the MCF10A cells (**Fig. 6c, Fig. S10**), the expression of several mesenchymal and epithelial markers (**Fig. 6d-e**), nor the viability of cells (**Fig. S2**). We hypothesize that if heparin treatment blocks MDA-TEV-induced EMT, then it may have an impact on cancer metastasis and could therefore be a putative starting point in developing an effective new drug for treating metastatic TNBC. An asymptotic regression was used to test if heparin treatment time significantly predicted the normalised cut-off frequency (**Fig. 6f**). The fitted regression model was:

$$\text{Normalised cut-off frequency} = \alpha - \beta \times \gamma^{\text{MDA-TEV treatment time}} \quad (2)$$

The overall regression was statistically significant ($R^2=.872$, $F(2,62)=210.63$, $p<.000$) and it was found that heparin treatment time significantly predicted normalised cut-off frequency ($\alpha=0.92$, $\beta=-3.52$, $\gamma=0.16$, $p=0.0013$), which compares well with the same model applied to the non-treated condition (**Fig. S5**). This demonstrates our ability to readily model the transient drug response and compare it to a control condition. Furthermore, it has been reported that persistent heparin treatment is necessary to abrogate the malignant effects of TEVs and inhibit TEV-induced tumour progression¹⁰⁷. To test the transient effect of heparin treatment, cells were concurrently treated with heparin and MDA-TEVs for 3 days, after which the

cells were washed in PBS and heparin treatment was ceased while MDA-TEV treatment continued (**Fig. 6g**). Our results confirm the transient effect of heparin treatment and demonstrate that persistent treatment of cells with heparin concurrently with exposure to MDA-TEVs is necessary to prevent MDA-TEV-induced EMT. This also demonstrates the ability of the OECT to continuously monitor drug response and investigate the temporal relationship between measured pharmacodynamic response and pharmacokinetics non-invasively and in a facile manner.

Outlook

Here, we demonstrate real-time, label-free, non-invasive monitoring of MDA-TEV-induced EMT using OECTs and produce quantitative time-series data that can be readily modelled to extract information on the kinetics governing TEV-driven epithelial barrier disruption. Our platform provides label-free high-content and multiparametric readouts of a transient pathological process, and we correlate the functional electrical measurements with biological readouts to establish a novel figure of merit for determining EMT status *in vitro*. Further, by employing OECT-based phenotypic drug screening, we identify heparin as a potent TEV-targeting, anti-EMT drug. Our approach provides continuous monitoring of therapeutic response in a dynamic and relevant cell-based disease model, enabling anti-metastatic drug screening that is facile and readily scalable for medium-high throughput operation.

By recapitulating a model of invasive ductal carcinoma and integrating it with OECTs, we developed a disease-relevant model amenable to probing by electrical measurements. This allowed us to capture the dynamics of MDA-TEV-induced EMT over a longer period of time, compared to studies using conventional cell-based assays^{76,77}, and allows integration of cells directly onto an electroactive substrate, for better compatibility with biomolecular assays. The compatibility of our platform with optical imaging and end-point biomolecular assays for multiparametric readouts is crucial for establishing OECT-based measurements as functional and robust figures of merit for EMT status, and is necessary for validation and qualification of analytical performance and biological *in vivo* relevance, and for adoption by industry and regulatory agencies²⁹. Further, our platform facilitates quantitative translation to *in vivo* outcomes, as it readily allows modelling of pharmacokinetic/pharmacodynamic (PK/PD) relationships to elucidate the causative relationship between drug exposure and response¹⁰⁸. . On the other hand, OECT monitoring represents a new tool for elucidating the role of TEVs in EMT and metastasis, with the potential to implicate specific EV subtypes, reveal dose-response relationships, and explore the function of EVs derived from cancerous/non-cancerous cell lines and clinical samples. Moreover, our platform is amenable to integration with models recapitulating other pathologies, where epithelial barrier function serves as a functional readout of pathogenesis/disease progression.

Given the high incidence and mortality rate of cancer, technologies that allow researchers to explore other therapeutic windows between normal and cancer cells that can be exploited to treat cancer and reduce the off-target effects of pharmacological modulation¹⁹ are required. Our platform could be used to explore pharmacological strategies against TEV dysregulation and aid the development of antimetastatic therapeutic strategies that target EMT.

Methods

Cell culture: MDA-MB-231 epithelial breast cancer cells (ATCC HTB-26) were cultured according to supplier's instructions with Dulbecco's Modified Eagle Medium (DMEM; Thermo Fisher Scientific, TFS) and supplemented with 10% (v/v) foetal bovine serum (FBS; Merck), 50 U/mL penicillin, 50 µg/mL streptomycin, and 1% (v/v) GlutaMAX (TFS). MDA-MB-231 cells were cultured to 80% confluency before passaging and did not exceed 15 passages. Human embryonic kidney 293 cells (HEK-293; kind gift from Marc Borsotto, Université de Nice Sophia Antipolis, France) were cultured with Advanced DMEM (TFS) and supplemented with 10% (v/v) FBS (Merck), 50 U/mL penicillin and 50 µg/mL streptomycin (TFS), 1% (v/v) GlutaMax (TFS), and 50 µg/mL gentamicin (TFS). HEK-293 cells were cultured to 70–80% confluency before passaging and did not exceed 15 passages. MCF10A human mammary epithelial cells (ATCC CRL-10317) were cultured according to supplier's instructions with Mammary Epithelial Cell Growth Medium Basal Medium (CC-3151; Lonza) and supplemented with growth supplements BPE, 2 ml; hEGF, 0.5 ml; Hydrocortisone, 0.5 ml; and insulin, 0.5 ml from MEGM SingleQuots Supplement Pack (CC-4136; Lonza) and 100 ng/ml cholera toxin (Sigma Aldrich). MCF10A were cultured to 70-80% confluency before passaging and did not exceed 10 passages and trypsin neutralising solution (TFS) was used during subculturing. All cell lines were incubated at 37 °C with 5% CO₂.

MCF10A cells display characteristics of luminal ductal cells but not of myoepithelial cells (**Fig. 1**) and they make up the mammary ductal microenvironment of the terminal ductal lobular unit, which is the origin of most pathologic breast lesions¹⁰⁹.

Isolation of EVs: For EV harvesting, MDA-MB-231 and HEK-293 cells were cultured until 80% confluent, washed twice with phosphate-buffered saline (PBS; TFS), and incubated with serum-free culture medium for 48 hours before the conditioned medium (CM) was collected for further processing. CM from MDA-MB-231 and HEK-293 cells was processed using a protocol adapted from¹¹⁰. In brief, CM was centrifuged at 4 °C, 3,000 $\times g$ for 30 min to remove cells and cellular debris. The supernatant was centrifuged at 4 °C, 100,000 $\times g$ for 4 h (Type 50.2 Ti Fixed-Angle Rotor, Beckmann XL-90 Ultracentrifuge) to pellet out EVs. The pellet was resuspended in 500 µL MCF10A cell culture medium or PBS (depending on the downstream application) and stored at 4 °C. For cell experiments, EVs were used within 2 days of isolation, and for particle imaging (TEM) and size analysis, EVs were analysed on the same day.

Transmission electron microscopy (TEM): Exosome samples were visualized by TEM using negative staining method. 10 µL sample was applied on glow-discharged carbon-coated copper grids for 2 min, washed twice in Milli-Q water for 30 s each, and stained with 1% (w/v) water solution of uranyl acetate for 2 min at RT. Imaging was performed on a FEI Tecnai G20 electron microscope, operating at 200 kV, 20 micron objective aperture, and images were recorded with an AMT camera.

Immunogold staining: TEVs from MDA-MB-231 cells were stained incubated with mouse anti-CD63 (TFS, 1:5 000) followed by anti-Ms conjugated with 20nm gold nanoparticle (1: 5000; TFS) for 2 hrs. TEVs were spun through a G25 column (Cytiva) after each incubation step and imaged using TEM.

EV size, concentration and zeta potential characterisation: Nanoparticle tracking analysis (NTA) was used to determine the size and particle concentration of EVs. Samples were diluted 100-fold in PBS and tracked on a Nanosight NS500 (Malvern). Zeta potential was determined using a folded capillary zeta cell (DTS1070, Malvern) and a Zetasizer Nano ZSP (Malvern). Samples were dispersed in PBS (pH 7.4) and the Smoluchowski model was applied.

Cell lysate and EV sample protein extraction: Cultured cells were washed twice with cold PBS and solubilised in 1 mL radio immunoprecipitation assay buffer (RIPA) Lysis and Extraction Buffer (TFS) supplemented with 10 µL Halt Protease Inhibitor Cocktail and 10 µL EDTA (TFS) immediately before use. Samples were incubated on ice for 5 min with agitation (20-30 min for MCF10A cells), aspirated buffer was collected into a microcentrifuge tube and centrifuged at 4 °C; 14,000 x *g* for 15 min to pellet cell debris. The supernatant (cell lysate) was collected and stored at -80 °C pending further analysis. EV protein samples were prepared by resuspending pellets post-ultracentrifugation in the supplemented RIPA buffer.

Western blot: The total protein content of cell lysates and EV samples was quantified using a Qubit 4 Fluorometer (TFS) per manufacturer's instruction. Samples were diluted in lithium dodecyl sulfate (LDS) sample buffer (4X Bolt; Invitrogen), denatured by heating for 10 min at 70 °C, and subjected to electrophoresis using precast NuPAGE Novex 4-12% Bis-Tris Proteins Gels (Invitrogen) in NuPAGE MES SDS Running Buffer (Invitrogen) under non-reducing conditions at constant 200 V for 30 min. The same amount of protein (between 10-25 µg) from each sample was loaded into the gel wells. Proteins were electrotransferred onto PVDF Transfer Membranes (TFS) using NuPAGE Transfer Buffer (Invitrogen). Membranes were blocked with 5% (w/v) BSA in PBS (TFS, Oxoid) with 0.1% (v/v) Tween-20 (PBST; TFS) for 1 h. For EV blots: Membranes were probed with mouse anti-CD9 (Invitrogen; 1:5 000), mouse anti-CD63 (TFS, 1:5 000), mouse anti-annexin A1 (TFS; 1:5 000), and rabbit anti-calreticulin (Abcam; 1:5 000) monoclonal primary antibodies for 1 h in PBST. For cell lysate blots: Membranes were probed with mouse anti-vimentin (Abcam; 1:1 000), mouse anti-F-actin (Abcam, 1:500), rabbit anti-E-cadherin (Abcam; 1:1 000), mouse anti-N-cadherin (1:1 000), mouse anti-TWIST1 (1:250), and mouse anti-GADPH (Sigma-Aldrich; 1:25 000) monoclonal primary antibodies for 1 h in PBST. This was followed by incubation with HRP-conjugated anti-mouse IgG H&L (Invitrogen; 1:10 000) and anti-rabbit IgG H&L (Abcam; 1:10 000) secondary antibodies in PBST for 1 h. All incubations were carried out on a shaker at RT or 4 °C. Western blots were washed 3-5 times in PBST for 5 min after each incubation step and were visualised using Pierce enhanced chemiluminescence (ECL) Western Blotting Substrate (TFS) on a G:BOX Chemi XX6 (Syngene). Band intensity was quantified using ImageJ Software Band function and normalised with GADPH to compare relative protein expression between conditions.

Cell-based EMT experiments in OECTs: OECTs were cleaned thoroughly with Milli-Q water and isopropanol prior to sterilising by immersion in 70% ethanol for 24 hours. The devices were left in a sterile MSC to promote evaporation of ethanol before incubating with normal culture medium overnight. Cloning cylinders with an area of 0.5 cm² doubled as culture wells which were stuck onto OECT devices with PDMS. The wells defined the area in which the cells were cultured, with 3-6 channels and a gate electrode

accessible within each well. MCF10A cells were then seeded at 1×10^4 cells/cm² and cultured for 3 days until cell coverage was ~70-80%, covering all channels fully, at which point the cells displayed a polygonal morphology, characteristic of an epithelial phenotype (**Fig 3a**). MCF10A cells are usually serum-starved for EMT studies⁷³ but the normal culture medium does not contain serum, therefore, the base medium was kept the same for all conditions. Treatment was started on day 3 (called treatment day 0) and cell culture media either pre-supplemented with 200 µg MDA-TEVs, 185 µg HEK-EVs, 10 ng/ml TGF-β1, heparin, or without supplementation. The discrepancy in dose between MDA-TEVs and HEK-EVs is due to the slight difference in protein-to-vesicle ratio of each EV type (see **Table 1**). EV dose, as measured by total protein content and correlated with vesicle concentration (see **Table 1**), was normalised to the number of MCF10A cells seeded to ensure that an equal number of cells were exposed to an equal number of EVs (in this case 12×10^9 vesicles per 5,000 cells seeded), regardless of culture area and medium volume. EV doses of 50-200 µg are typical^{77,111,112} and a 5 ng/ml dose of TGF-β1 induces EMT in MCF10A cells⁷³, but prolonged treatment with 5 ng/ml TGF-β1 (6 days) is necessary to induce EMT in MCF10A cells⁷², therefore the dose was increased to 10 ng/ml¹¹³ to accelerate this process. Supplemented exogenous EVs were isolated from their respective cell lines every 2 days and used fresh to prevent degradation of EV function by prolonged storage times. Electrical measurements were performed prior to medium changes. Cells in the OECTs were either fixed for immunofluorescence (IF) staining or lysed to collect whole-cell lysates for immunoblot analysis on treatment day 9 (after 12 days of culture). Experiments were also performed in 100 mm petri dishes and 24-well plates in parallel with OECT experiments.

Heparin treatment. Cells were incubated with or without 200 µg MDA-TEVs in the presence or absence of 10 µg/ml^{4,7,105} heparin sodium salt from porcine intestinal mucosa (Sigma-Aldrich). Heparin treatment was refreshed every 48 hours concurrently with medium changes (supplemented with MDA-TEVs or not). In the transient heparin treatment study, cells were treated with MDA-TEVs and heparin concurrently until day 3, after which time the cells were washed thoroughly with PBS three times¹⁰⁵ and treated with MDA-TEVs for the remainder of the experiment.

Fabrication of OECTs: OECTs were microfabricated on glass substrates based on established protocols using standard photolithography and parylene C peel-off techniques^{114,115}. The process starts with the first layer of photoresist (AZ5214) being spin coated and exposed to ultraviolet light using contact aligner to create Au electrodes and interconnection pads. The photoresist patterns were generated with AZ 726 MIF developer, followed by metal sputtering of 10 nm Cr and 100 nm Au and a standard lift-off process using hot dimethyl sulfoxide. Next, we coated the second layer of photoresist AZ9260 on the substrates and developed them using AZ developer. A parylene C layer was deposited to insulate the gold interconnects. The OECT channel and gate were patterned by reactive ion etching, using a second layer of parylene C, which was peeled off to yield a channel length and width of 50 µm or 100 µm and a gate dimension of 500 x 500 µm².

Organic Electrochemical Transistor Measurements: OECTs were characterized using a dual-channel source-meter unit (NI-PXI) with custom-written control code in LabVIEW. All measurements were performed using the integrated planar gate electrodes. The channels studied were either 50x50 μm or 100x100 μm in length and width.

Extraction of cell layer resistance from Z vs frequency plots: The electrochemical impedance spectra (EIS) was obtained from the OECT channels using the source, drain and gate as the three electrode setup and a custom made MATLAB code as described earlier by Rivnay et al⁷⁰. EIS was performed at a frequency range between 100 kHz to 0.1 Hz at $V = 0\text{ V vs } V_{\text{OC}}$ with an AC amplitude of 10 mV. We extracted the resistance value for each condition by using equation 1 and the impedance magnitude value at 2 kHz, assuming that capacitance contribution to the overall signal is negligible.

$$Z = \sqrt{R^2 + \frac{1}{\omega^2 C^2}} \quad (3)$$

OECT data analysis: Cut-off frequency (CF) was normalised to treatment start date using the following equation: *Normalised CF* = $CF_n/CF_{n=0}$, where n is treatment day and $CF_{n=0}$ refers to the cut-off frequency on treatment day 0.

Confocal Microscopy: *Viability assay:* the viability of cells growing on the OECT platform was checked by evaluating plasma membrane intactness and enzymatic activity via a two-colour fluorescence cytotoxicity/viability assay (LIVE/DEAD™ Viability/Cytotoxicity Kit, for mammalian cells, Invitrogen). The assay was performed at the end of the experimental period (culture day 12), by removing cell growth medium, washing thoroughly with PBS and adding the reagents. After 1-hour incubation, the reagent was replaced with PBS before visualization with a confocal microscope. *Immunofluorescence staining:* All samples were fixed with 4% paraformaldehyde (PFA, ThermoFisher Scientific) for 10 min, at room temperature; then, samples were thoroughly washed with PBS and stored at 4 °C until ready to use. Prior to immunofluorescently labelling the samples, cells were permeabilized in 0.1% v/v Triton X-100 (Fisher) for 10 min and then blocked for nonspecific binding with 1% wt/v BSA (TFS) and 0.1% v/v Tween-20 (TFS) in PBS for 1 hour at room temperature. The primary and secondary antibodies used are: Phalloidin-iFluor 594 Reagent (abcam), Bisbenzamide H (Hoechst 33342) (abcam). Images were obtained using an epifluorescence/confocal microscope (Axio Observer Z1 LSM 800, Zeiss), using 10x/0.45 and 20x/0.8, (Plan-Apochromat, Zeiss) objective. The 2D micrographs shown are representative of three different frames/locations of each. *Z-stacks and cell height:* For each condition/treatment, z-stacked confocal images were acquired from at least one channel of the respective OECT devices (independent samples). After acquiring these, the height of cells on the OECT channel was measured using the ortho-view (x/z and y/z planes) and graphic features/tools of the confocal microscope software (Axio Observer Z1 LSM 800, Zeiss; ZEN blue edition 3.4). The mean cell height for each condition/channel/sample was calculated from at least eight measurements: the z plane was fixed in the middle/center of each cell layer on the

respective OECT channel, as identified by the z-stack series data, and x and y locations were varied within this frame to account for variations of the cell layer height on this surface/plane.

Enzyme-linked immunosorbent assay (ELISA): To investigate the expression of mesenchymal marker N-cadherin in MCF10A cells before and after treatment with MDA-TEVs, an ELISA assay was done. Following the manufacturer's protocol, a Human N-cadherin DuoSet ELISA kit (R&D Systems) was utilized to measure the concentration of N-cadherin in MCF10A lysates on day 7 of treatment. Absorbance at 450 nm, as recommended, was measured for all samples, and the concentration of N-cadherin was found using the absorbance and concentration of the protein standards and the absorbance of the unknown concentration samples. The concentration of N-cadherin protein present in MCF10A lysates was normalized by total protein content.

Cell density from IF micrographs: IF images were analysed using ImageJ software. Cell count was performed using the software. Images were converted to 8-bit, and the threshold was adjusted to minimise noise and amplify contrast. The binary tools Fill Holes and Watershed were used to automatically determine cell borders. Cells were automatically counted using the Analyze Particles tool. Both cell counts including and excluding image borders were performed, and their mean was used as the final cell count.

DNA extraction and methylation qPCR: QIAamp DNA mini kit (Qiagen) was used to extract DNA from TEV-treated un-treated MCF10A cells according to the manufacturer's protocol. A total DNA input of 300 ng was bisulfite converted using the EZ DNA Methylation Gold kit (Zymo) following manufacturer's protocol. For the qPCR assay, a TaqMan approach was used involving gene-specific primers and probe targeting the methylated sequences. No amplification detected was considered to be non-methylated DNA for the target. Each sample was run in triplicate for the two genes; TWIST1 and TFPI2, and for the house-keeper gene B-actin used to control for variances in DNA input. A standard curve was initially established using fully methylated DNA (Merck), and each subsequent qPCR run included a calibrator (1:100 dilution) to allow for quantification and negative controls.

Each PCR contained a final concentration of 1x LightCycler Probes (Roche), 0.6 µM each primer, 0.2 µM probe, 2.5% DMSO, 1M betaine and 2 µL bisulfite converted DNA in a final reaction volume of 10 µL. Reactions were carried out using a LightCycler 480II (Roche) using the following qPCR thermal cycling conditions; 95°C for 10 mins, 50 cycles of 95°C for 15 sec, 60 °C for 60 sec including data acquisition. Methylation was determined as previously described by Chettouh et al., (2018):

$$\text{Total Methylation (\%)} = \sum \frac{\left(\frac{A}{B}\right)}{\left(\frac{C}{D}\right)} \quad (4)$$

A= methylation value of gene of interest in each sample; B = methylation value of the gene of interest in the calibrator; C= amplification value of β actin in each sample; and D= amplification value of β actin in

the calibrator.

Sequence Name	Nucleotide Sequence
TWIST1_Forward	CGTCTACAACCTCCTCGTAAACTACG
TWIST1_Reverse	TCGGGTAGTTCGGTTTAGGGTAAG
TWIST1_Probe	[6FAM]ACTCCCGCCGCGCTACTACTACC[TAM]
TFPI2_Forward	TGTAGGGGGTCTGGGCGGTTC
TFPI2_Reverse	CGCTCGCCCCGCATAAAACG
TFPI2_Probe	[6FAM]CGTTTGGCGGGAGGAGGTGCGCGGTT[TAM]
Beta-actin_Forward	TGGTGATGGAGGAGGTTTAGTAAGT
Beta-actin Reverse	AACCAATAAACCTACTCCTCCCTTAA
Beta-actin_Probe	[6FAM]ACCACCACCCAACACACAATAACAAACACA[TAM]

Statistical Analysis: For all experiments performed in this study, variance analysis was performed using a one-way or two-way ANOVA, depending on the number of factors, to find significant differences between conditions. F- and p-value were reported using the following convention: F(df regression, df residual) = [F-value], p = [p-value]. All data were plotted and analysed using Microsoft Excel and OriginLab Pro and they were presented as mean ± s.e.m. Statistical significance levels were determined as follows: *p ≤ 0.05, **p ≤ 0.01, and ***p ≤ 0.001. Each biological independent experiments correspond to biological replicates where cells from different passages were used; n = total number of biological replicates.

Declarations

Acknowledgements

This publication was supported by the King Abdullah University of Science and Technology (KAUST) Office of Sponsored Research (OSR) under Award No. OSR-2018-CRG7-3709. W.C.T. acknowledges funding from the Cambridge Commonwealth, European & International Trust and Churchill College at Cambridge University. J.U. acknowledges funding from the National Science Foundation Graduate Research Fellowship [Grant Number DGE-1650441], and the Sloan Foundation (Grant number 70481). R.M. acknowledges funding from EPSRC Cambridge NanoDTC under award EP/S022953/1. S.P. acknowledges funding from Cambridge Commonwealth, European & International Trust and Trinity College at Cambridge University and Sensors CDT from EPSRC funding by the Engineering and Physical Sciences Research Council Centre for Doctoral Training in Sensor Technologies and Applications (EP/L015889/1).

Schematic 1 and Figure 6a were created with Biorender.com and elements of the former were adapted from “Breast Cancer to Brain Metastasis” (2020). The authors gratefully acknowledge the Cambridge Advanced Imaging Centre for their support & assistance with transmission electron microscope imaging.

Competing interests

None

References

1. Thiery, J. P., Acloque, H., Huang, R. Y. J. & Nieto, M. A. Epithelial-Mesenchymal Transitions in Development and Disease. *Cell* **139**, 871–890 (2009).
2. You, Y. *et al.* Matrix metalloproteinase 13-containing exosomes promote nasopharyngeal carcinoma metastasis. *Cancer Sci.* **106**, 1669–1677 (2015).
3. Cha, D. J. *et al.* KRAS-dependent sorting of miRNA to exosomes. *eLife* **4**, e07197 (2015).
4. Franzen, C. A. *et al.* Urothelial cells undergo epithelial-to-mesenchymal transition after exposure to muscle invasive bladder cancer exosomes. *Oncogenesis* **4**, e163–e163 (2015).
5. Kucharzewska, P. *et al.* Exosomes reflect the hypoxic status of glioma cells and mediate hypoxia-dependent activation of vascular cells during tumor development. *Proc. Natl. Acad. Sci.* **110**, 7312–7317 (2013).
6. Zhou, W. *et al.* Cancer-Secreted miR-105 Destroys Vascular Endothelial Barriers to Promote Metastasis. *Cancer Cell* **25**, 501–515 (2014).
7. Christianson, H. C., Svensson, K. J., van Kuppevelt, T. H., Li, J.-P. & Belting, M. Cancer cell exosomes depend on cell-surface heparan sulfate proteoglycans for their internalization and functional activity. *Proc. Natl. Acad. Sci.* **110**, 17380–17385 (2013).
8. Costa-Silva, B. *et al.* Pancreatic cancer exosomes initiate pre-metastatic niche formation in the liver. *Nat. Cell Biol.* **17**, 816–826 (2015).
9. Mao, Y. *et al.* Hypoxic exosomes facilitate angiogenesis and metastasis in esophageal squamous cell carcinoma through altering the phenotype and transcriptome of endothelial cells. *J. Exp. Clin. Cancer Res.* **38**, 389 (2019).
10. Clayton, A., Al-Taei, S., Webber, J., Mason, M. D. & Tabi, Z. Cancer Exosomes Express CD39 and CD73, Which Suppress T Cells through Adenosine Production. *J. Immunol.* **187**, 676–683 (2011).
11. Fabbri, M. *et al.* MicroRNAs bind to Toll-like receptors to induce prometastatic inflammatory response. *Proc. Natl. Acad. Sci.* **109**, (2012).
12. Fares, J., Fares, M. Y., Khachfe, H. H., Salhab, H. A. & Fares, Y. Molecular principles of metastasis: a hallmark of cancer revisited. *Signal Transduct. Target. Ther.* **5**, 1–17 (2020).
13. Qian, C.-N., Mei, Y. & Zhang, J. Cancer metastasis: issues and challenges. *Chin. J. Cancer* **36**, 38 (2017).

14. Wouters, O. J., McKee, M. & Luyten, J. Estimated Research and Development Investment Needed to Bring a New Medicine to Market, 2009–2018. *JAMA* **323**, 844–853 (2020).
15. Wong, C. H., Siah, K. W. & Lo, A. W. Estimation of clinical trial success rates and related parameters. *Biostatistics* **20**, 273–286 (2019).
16. Harrison, R. K. Phase II and phase III failures: 2013–2015. *Nat. Rev. Drug Discov.* **15**, 817–818 (2016).
17. Gui, P. & Bivona, T. G. Evolution of metastasis: new tools and insights. *Trends Cancer* **8**, 98–109 (2022).
18. Hasan, H. *et al.* Extracellular vesicles released by non-small cell lung cancer cells drive invasion and permeability in non-tumorigenic lung epithelial cells. *Sci. Rep.* **12**, 972 (2022).
19. Syn, N., Wang, L., Sethi, G., Thiery, J.-P. & Goh, B.-C. Exosome-Mediated Metastasis: From Epithelial–Mesenchymal Transition to Escape from Immunosurveillance. *Trends Pharmacol. Sci.* **37**, 606–617 (2016).
20. Rodríguez, M. *et al.* Exosomes enriched in stemness/metastatic-related mRNAs promote oncogenic potential in breast cancer. *Oncotarget* **6**, 40575–40587 (2015).
21. Melo, S. A. *et al.* Cancer Exosomes Perform Cell-Independent MicroRNA Biogenesis and Promote Tumorigenesis. *Cancer Cell* **26**, 707–721 (2014).
22. Thiery, J. P. Epithelial–mesenchymal transitions in tumour progression. *Nat. Rev. Cancer* **2**, 442–454 (2002).
23. Hanahan, D. & Weinberg, R. A. Hallmarks of Cancer: The Next Generation. *Cell* **144**, 646–674 (2011).
24. Lener, T. *et al.* Applying extracellular vesicles based therapeutics in clinical trials – an ISEV position paper. *J. Extracell. Vesicles* **4**, (2015).
25. Moffat, J. G., Vincent, F., Lee, J. A., Eder, J. & Prunotto, M. Opportunities and challenges in phenotypic drug discovery: an industry perspective. *Nat. Rev. Drug Discov.* **16**, 531–543 (2017).
26. Menyhárt, O. *et al.* Guidelines for the selection of functional assays to evaluate the hallmarks of cancer. *Biochim. Biophys. Acta BBA - Rev. Cancer* **1866**, 300–319 (2016).
27. Kumar, N., Afjei, R., Massoud, T. F. & Paulmurugan, R. Comparison of cell-based assays to quantify treatment effects of anticancer drugs identifies a new application for Bodipy-L-cystine to measure apoptosis. *Sci. Rep.* **8**, 16363 (2018).
28. McAleer, C. W. *et al.* On the potential of in vitro organ-chip models to define temporal pharmacokinetic-pharmacodynamic relationships. *Sci. Rep.* **9**, 9619 (2019).
29. Low, L. A., Mummery, C., Berridge, B. R., Austin, C. P. & Tagle, D. A. Organs-on-chips: into the next decade. *Nat. Rev. Drug Discov.* **20**, 345–361 (2021).
30. Twenty-five years of conducting polymers. *Chem. Commun.* **0**, 1–4 (2003).
31. Ramuz, M. *et al.* Combined Optical and Electronic Sensing of Epithelial Cells Using Planar Organic Transistors. *Adv. Mater.* **26**, 7083–7090 (2014).

32. Curto, V. F. *et al.* Organic transistor platform with integrated microfluidics for in-line multi-parametric in vitro cell monitoring. *Microsyst. Nanoeng.* **3**, 17028 (2017).
33. Jimison, L. H. *et al.* Measurement of Barrier Tissue Integrity with an Organic Electrochemical Transistor. *Adv. Mater.* **24**, 5919–5923 (2012).
34. Pappa, A.-M. *et al.* Optical and Electronic Ion Channel Monitoring from Native Human Membranes. *ACS Nano* (2020) doi:10.1021/acsnano.0c01330.
35. Tang, T. *et al.* Functional Infectious Nanoparticle Detector: Finding Viruses by Detecting Their Host Entry Functions Using Organic Bioelectronic Devices. *ACS Nano* **15**, 18142–18152 (2021).
36. Moysidou, C.-M. *et al.* 3D Bioelectronic Model of the Human Intestine. *Adv. Biol.* **5**, 2000306 (2021).
37. Inal, S. *et al.* Conducting Polymer Scaffolds for Hosting and Monitoring 3D Cell Culture. *Adv. Biosyst.* **1**, 1700052 (2017).
38. Rivnay, J. *et al.* Organic electrochemical transistors. *Nat. Rev. Mater.* **3**, 1–14 (2018).
39. Zhang, Y. *et al.* Supported Lipid Bilayer Assembly on PEDOT:PSS Films and Transistors. *Adv. Funct. Mater.* **26**, 7304–7313 (2016).
40. Friedlein, J. T., McLeod, R. R. & Rivnay, J. Device physics of organic electrochemical transistors. *Org. Electron.* **63**, 398–414 (2018).
41. Bernards, D. A. & Malliaras, G. G. Steady-State and Transient Behavior of Organic Electrochemical Transistors. *Adv. Funct. Mater.* **17**, 3538–3544 (2007).
42. Rivnay, J. *et al.* High-performance transistors for bioelectronics through tuning of channel thickness. *Sci. Adv.* **1**, e1400251 (2015).
43. Khodagholy, D. *et al.* High transconductance organic electrochemical transistors. *Nat. Commun.* **4**, 2133 (2013).
44. Rivnay, J. *et al.* Organic Electrochemical Transistors with Maximum Transconductance at Zero Gate Bias. *Adv. Mater.* **25**, 7010–7014 (2013).
45. Dijk, G., Rutz, A. L. & Malliaras, G. G. Stability of PEDOT:PSS-Coated Gold Electrodes in Cell Culture Conditions. *Adv. Mater. Technol.* **5**, 1900662 (2020).
46. Savva, A., Wustoni, S. & Inal, S. Ionic-to-electronic coupling efficiency in PEDOT:PSS films operated in aqueous electrolytes. *J. Mater. Chem. C* **6**, 12023–12030 (2018).
47. Proctor, C. M., Rivnay, J. & Malliaras, G. G. Understanding volumetric capacitance in conducting polymers. *J. Polym. Sci. Part B Polym. Phys.* **54**, 1433–1436 (2016).
48. Ramuz, M., Hama, A., Rivnay, J., Leleux, P. & Owens, R. M. Monitoring of cell layer coverage and differentiation with the organic electrochemical transistor. *J. Mater. Chem. B* **3**, 5971–5977 (2015).
49. Rivnay, J. *et al.* Using white noise to gate organic transistors for dynamic monitoring of cultured cell layers. *Sci. Rep.* **5**, 11613 (2015).
50. Fariat, G. C. *et al.* Organic electrochemical transistors as impedance biosensors. *MRS Commun.* **4**, 189–194 (2014).

51. Huerta, M., Rivnay, J., Ramuz, M., Hama, A. & Owens, R. M. Early Detection of Nephrotoxicity In Vitro Using a Transparent Conducting Polymer Device. *Appl. Vitro Toxicol.* **2**, 17–25 (2016).
52. Lieberth, K. *et al.* Monitoring Reversible Tight Junction Modulation with a Current-Driven Organic Electrochemical Transistor. *Adv. Mater. Technol.* **6**, 2000940 (2021).
53. Yeung, S. Y., Gu, X., Tsang, C. M., Tsao, S. W. G. & Hsing, I. Organic electrochemical transistor array for monitoring barrier integrity of epithelial cells invaded by nasopharyngeal carcinoma. *Sens. Actuators B Chem.* **297**, 126761 (2019).
54. Qu, Y. *et al.* Evaluation of MCF10A as a Reliable Model for Normal Human Mammary Epithelial Cells. *PLOS ONE* **10**, e0131285 (2015).
55. Puleo, J. & Polyak, K. The MCF10 Model of Breast Tumor Progression. *Cancer Res.* **81**, 4183–4185 (2021).
56. Liu, K. *et al.* Evaluating cell lines as models for metastatic breast cancer through integrative analysis of genomic data. *Nat. Commun.* **10**, 2138 (2019).
57. Théry, C. *et al.* Minimal information for studies of extracellular vesicles 2018 (MISEV2018): a position statement of the International Society for Extracellular Vesicles and update of the MISEV2014 guidelines. *J. Extracell. Vesicles* **7**, 1535750 (2018).
58. Jeppesen, D. K. *et al.* Reassessment of Exosome Composition. *Cell* **177**, 428–445.e18 (2019).
59. Melo, S. A. *et al.* Glypican-1 identifies cancer exosomes and detects early pancreatic cancer. *Nature* **523**, 177–182 (2015).
60. Szczepanski, M. J., Szajnik, M., Welsh, A., Whiteside, T. L. & Boyiadzis, M. Blast-derived microvesicles in sera from patients with acute myeloid leukemia suppress natural killer cell function via membrane-associated transforming growth factor- β 1. *Haematologica* **96**, 1302–1309 (2011).
61. King, H. W., Michael, M. Z. & Gleadle, J. M. Hypoxic enhancement of exosome release by breast cancer cells. *BMC Cancer* **12**, 421 (2012).
62. Uribe, J. *et al.* Dual Mode Sensing of Binding and Blocking of Cancer Exosomes to Biomimetic Human Primary Stem Cell Surfaces. *ACS Biomater. Sci. Eng.* (2021) doi:10.1021/acsbiomaterials.1c01056.
63. Kowal, E. J. K., Ter-Ovanesyan, D., Regev, A. & Church, G. M. Extracellular Vesicle Isolation and Analysis by Western Blotting. in *Extracellular Vesicles: Methods and Protocols* (eds. Kuo, W. P. & Jia, S.) 143–152 (Springer, 2017). doi:10.1007/978-1-4939-7253-1_12.
64. Srinivasan, B. *et al.* TEER measurement techniques for in vitro barrier model systems. *J. Lab. Autom.* **20**, 107–126 (2015).
65. Shintani, Y., Maeda, M., Chaika, N., Johnson, K. R. & Wheelock, M. J. Collagen I Promotes Epithelial-to-Mesenchymal Transition in Lung Cancer Cells via Transforming Growth Factor- β Signaling. *Am. J. Respir. Cell Mol. Biol.* **38**, 95–104 (2008).
66. Vellinga, T. T. *et al.* Collagen-rich stroma in aggressive colon tumors induces mesenchymal gene expression and tumor cell invasion. *Oncogene* **35**, 5263–5271 (2016).

67. Kaiser, J.-P. *et al.* Cytotoxic effects of nanosilver are highly dependent on the chloride concentration and the presence of organic compounds in the cell culture media. *J. Nanobiotechnology* **15**, 5 (2017).
68. Kolli, R., Kaivosoja, E. & Levon, K. Choice of Reference Electrode is Critical for Potentiometric Whole Cell-based Sensor. *Electroanalysis* **27**, 1636–1641 (2015).
69. Tria, S. A. *et al.* Dynamic Monitoring of Salmonella typhimurium Infection of Polarized Epithelia Using Organic Transistors. *Adv. Healthc. Mater.* **3**, 1053–1060 (2014).
70. Rivnay, J. *et al.* Organic electrochemical transistors for cell-based impedance sensing. *Appl. Phys. Lett.* **106**, 043301 (2015).
71. Xu, J., Lamouille, S. & Derynck, R. TGF- β -induced epithelial to mesenchymal transition. *Cell Res.* **19**, 156–172 (2009).
72. Brown, K. A. *et al.* Induction by transforming growth factor- β 1 of epithelial to mesenchymal transition is a rare event in vitro. *Breast Cancer Res.* **6**, R215 (2004).
73. Mori, S. *et al.* Enhanced Expression of Integrin α v β 3 Induced by TGF- β Is Required for the Enhancing Effect of Fibroblast Growth Factor 1 (FGF1) in TGF- β -Induced Epithelial-Mesenchymal Transition (EMT) in Mammary Epithelial Cells. *PLOS ONE* **10**, e0137486 (2015).
74. Yang, J. *et al.* Guidelines and definitions for research on epithelial–mesenchymal transition. *Nat. Rev. Mol. Cell Biol.* **21**, 341–352 (2020).
75. Grände, M. *et al.* Transforming growth factor- β and epidermal growth factor synergistically stimulate epithelial to mesenchymal transition (EMT) through a MEK-dependent mechanism in primary cultured pig thyrocytes. *J. Cell Sci.* **115**, 4227–4236 (2002).
76. Galindo-Hernandez, O., Serna-Marquez, N., Castillo-Sanchez, R. & Salazar, E. P. Extracellular vesicles from MDA-MB-231 breast cancer cells stimulated with linoleic acid promote an EMT-like process in MCF10A cells. *Prostaglandins Leukot. Essent. Fatty Acids* **91**, 299–310 (2014).
77. Leal-Orta, E., Ramirez-Ricardo, J., Garcia-Hernandez, A., Cortes-Reynosa, P. & Salazar, E. P. Extracellular vesicles from MDA-MB-231 breast cancer cells stimulated with insulin-like growth factor 1 mediate an epithelial–mesenchymal transition process in MCF10A mammary epithelial cells. *J. Cell Commun. Signal.* (2021) doi:10.1007/s12079-021-00638-y.
78. Verma, R. Fibronectin. in *Encyclopedia of Cancer* (ed. Schwab, M.) 1399–1402 (Springer, 2011). doi:10.1007/978-3-642-16483-5_2182.
79. He, P., Qiu, K. & Jia, Y. Modeling of mesenchymal hybrid epithelial state and phenotypic transitions in EMT and MET processes of cancer cells. *Sci. Rep.* **8**, 14323 (2018).
80. Reyngold, M. *et al.* Remodeling of the Methylation Landscape in Breast Cancer Metastasis. *PLOS ONE* **9**, e103896 (2014).
81. Chimonidou, M. *et al.* DNA Methylation of Tumor Suppressor and Metastasis Suppressor Genes in Circulating Tumor Cells. *Clin. Chem.* **57**, 1169–1177 (2011).

82. Baylin, S. B. & Jones, P. A. A decade of exploring the cancer epigenome – biological and translational implications. *Nat. Rev. Cancer* **11**, 726–734 (2011).
83. Cheng, Y. *et al.* Targeting epigenetic regulators for cancer therapy: mechanisms and advances in clinical trials. *Signal Transduct. Target. Ther.* **4**, 1–39 (2019).
84. Zhu, X. *et al.* BCR-ABL1–positive microvesicles transform normal hematopoietic transplants through genomic instability: implications for donor cell leukemia. *Leukemia* **28**, 1666–1675 (2014).
85. Zhao, D. *et al.* TFPI2 suppresses breast cancer progression through inhibiting TWIST-integrin $\alpha 5$ pathway. *Mol. Med.* **26**, 27 (2020).
86. Guo, H. *et al.* Tissue factor pathway inhibitor-2 was repressed by CpG hypermethylation through inhibition of KLF6 binding in highly invasive breast cancer cells. *BMC Mol. Biol.* **8**, 110 (2007).
87. Eads, C. A. *et al.* MethyLight: a high-throughput assay to measure DNA methylation. *Nucleic Acids Res.* **28**, e32-00 (2000).
88. Chettouh, H. *et al.* Methylation panel is a diagnostic biomarker for Barrett’s oesophagus in endoscopic biopsies and non-endoscopic cytology specimens. *Gut* **67**, 1942–1949 (2018).
89. Nairismägi, M.-L. *et al.* Translational control of TWIST1 expression in MCF-10A cell lines recapitulating breast cancer progression. *Oncogene* **31**, 4960–4966 (2012).
90. Zhan, Y. *et al.* Carcinoma-associated fibroblasts derived exosomes modulate breast cancer cell stemness through exonic circHIF1A by miR-580-5p in hypoxic stress. *Cell Death Discov.* **7**, 1–15 (2021).
91. Tan, E.-J. *et al.* Regulation of transcription factor Twist expression by the DNA architectural protein high mobility group A2 during epithelial-to-mesenchymal transition. *J. Biol. Chem.* **287**, 7134–7145 (2012).
92. Ramesh, V., Brabletz, T. & Ceppi, P. Targeting EMT in Cancer with Repurposed Metabolic Inhibitors. *Trends Cancer* **6**, 942–950 (2020).
93. Jonckheere, S. *et al.* Epithelial-Mesenchymal Transition (EMT) as a Therapeutic Target. *Cells Tissues Organs* **211**, 157–182 (2022).
94. Dudás, J., Ladányi, A., Ingruber, J., Steinbichler, T. B. & Riechelmann, H. Epithelial to Mesenchymal Transition: A Mechanism that Fuels Cancer Radio/Chemo-resistance. *Cells* **9**, 428 (2020).
95. Garcia, E. *et al.* Inhibition of triple negative breast cancer metastasis and invasiveness by novel drugs that target epithelial to mesenchymal transition. *Sci. Rep.* **11**, 11757 (2021).
96. Saxena, M., Stephens, M. A., Pathak, H. & Rangarajan, A. Transcription factors that mediate epithelial–mesenchymal transition lead to multidrug resistance by upregulating ABC transporters. *Cell Death Dis.* **2**, e179–e179 (2011).
97. Pattabiraman, D. R. *et al.* Activation of PKA leads to mesenchymal-to-epithelial transition and loss of tumor-initiating ability. *Science* **351**, aad3680 (2016).
98. Van Noorden, C. J. F., van Sluis, G. L. & Spek, C. A. Experimental and clinical effects of anticoagulants on cancer progression. *Thromb. Res.* **125**, S77–S79 (2010).

99. Gerotziafas, G. T., Papageorgiou, C., Hatmi, M., Samama, M.-M. & Elalamy, I. Clinical Studies with Anticoagulants to Improve Survival in Cancer Patients. *Pathophysiol. Haemost. Thromb.* **36**, 204–211 (2007).
100. Hejna, M., Raderer, M. & Zielinski, C. C. Inhibition of Metastases by Anticoagulants. *JNCI J. Natl. Cancer Inst.* **91**, 22–36 (1999).
101. Alyahya, R., Sudha, T., Racz, M., Stain, S. C. & Mousa, S. A. Anti-metastasis efficacy and safety of non-anticoagulant heparin derivative versus low molecular weight heparin in surgical pancreatic cancer models. *Int. J. Oncol.* **46**, 1225–1231 (2015).
102. Niers, T. M. H. *et al.* Mechanisms of heparin induced anti-cancer activity in experimental cancer models. *Crit. Rev. Oncol. Hematol.* **61**, 195–207 (2007).
103. Borsig, L. *et al.* Heparin and cancer revisited: Mechanistic connections involving platelets, P-selectin, carcinoma mucins, and tumor metastasis. *Proc. Natl. Acad. Sci.* **98**, 3352–3357 (2001).
104. Mei, L. *et al.* Antitumor and Antimetastasis Activities of Heparin-based Micelle Served As Both Carrier and Drug. *ACS Appl. Mater. Interfaces* **8**, 9577–9589 (2016).
105. Atai, N. A. *et al.* Heparin blocks transfer of extracellular vesicles between donor and recipient cells. *J. Neurooncol.* **115**, 343–351 (2013).
106. Franzen, C. A. *et al.* Characterization of Uptake and Internalization of Exosomes by Bladder Cancer Cells. *BioMed Res. Int.* 2014, e619829 (2014).
107. Sento, S., Sasabe, E. & Yamamoto, T. Application of a Persistent Heparin Treatment Inhibits the Malignant Potential of Oral Squamous Carcinoma Cells Induced by Tumor Cell-Derived Exosomes. *PLOS ONE* **11**, e0148454 (2016).
108. Derendorf, H. *et al.* Pharmacokinetic/pharmacodynamic modeling in drug research and development. *J. Clin. Pharmacol.* **40**, 1399–1418 (2000).
109. Cichon, M. A., Degnim, A. C., Visscher, D. W. & Radisky, D. C. Microenvironmental Influences that Drive Progression from Benign Breast Disease to Invasive Breast Cancer. *J. Mammary Gland Biol. Neoplasia* **15**, 389–397 (2010).
110. Risha, Y., Minic, Z., Ghobadloo, S. M. & Berezovski, M. V. The proteomic analysis of breast cell line exosomes reveals disease patterns and potential biomarkers. *Sci. Rep.* **10**, 13572 (2020).
111. Otero-Ortega, L. *et al.* Low dose of extracellular vesicles identified that promote recovery after ischemic stroke. *Stem Cell Res. Ther.* **11**, 70 (2020).
112. Yin, Y., Shelke, G. V., Lässer, C., Brismar, H. & Lötvall, J. Extracellular vesicles from mast cells induce mesenchymal transition in airway epithelial cells. *Respir. Res.* **21**, 101 (2020).
113. Pell, T. J. *et al.* Epithelial Barrier Integrity Profiling: Combined Approach Using Cellular Junctional Complex Imaging and Transepithelial Electrical Resistance. *SLAS Discov.* **26**, 909–921 (2021).
114. Wustoni, S., Savva, A., Sun, R., Bihar, E. & Inal, S. Enzyme-Free Detection of Glucose with a Hybrid Conductive Gel Electrode. *Adv. Mater. Interfaces* **6**, 1800928 (2019).

115. Ohayon, D. *et al.* Biofuel powered glucose detection in bodily fluids with an n-type conjugated polymer. *Nat. Mater.* **19**, 456–463 (2020).

Figures

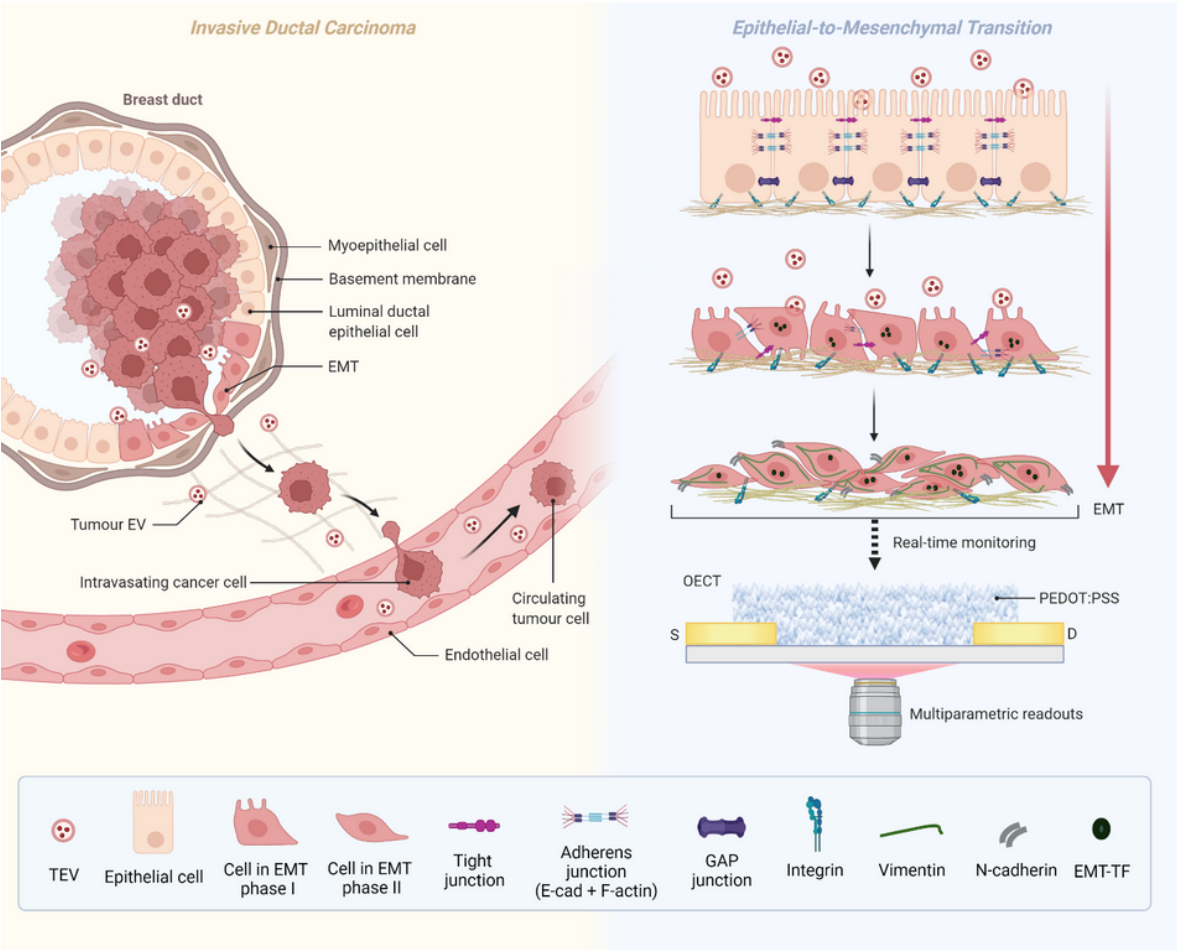


Figure 1

Schematic 1: A model to recapitulate invasive ductal carcinoma integrated with an OECT platform for investigating TEV-induced EMT. EMT has been implicated in the initiation of metastasis, as epithelial cells at the invasive front of carcinomas acquire migratory and invasive properties to break through the basement membrane and disseminate via circulation to form metastases in distal organs¹. Post-internalisation, recipient cells exhibit physiological changes associated with alterations of their

transcriptome and proteome^{2,3}. TEV exposure results in increased expression of several mesenchymal markers, including α -smooth muscle actin and Snail⁴, decreased expression of epithelial markers, including β -catenin⁵ and tight junction protein ZO-1⁶, and reciprocal changes in E-cadherin and N-cadherin expression² – the so-called cadherin switch. Functionally, TEVs enhance the migratory and invasive properties of recipient cells^{4,7}. TEVs may further facilitate premetastatic niche formation⁸, promote angiogenesis⁹, alter host immune response¹⁰, and induce pro-metastatic inflammatory response¹¹. By integrating a highly relevant model of breast cancer metastasis associated EMT on OECTs, we unlock real-time monitoring of this malignant process with multiparametric readouts.

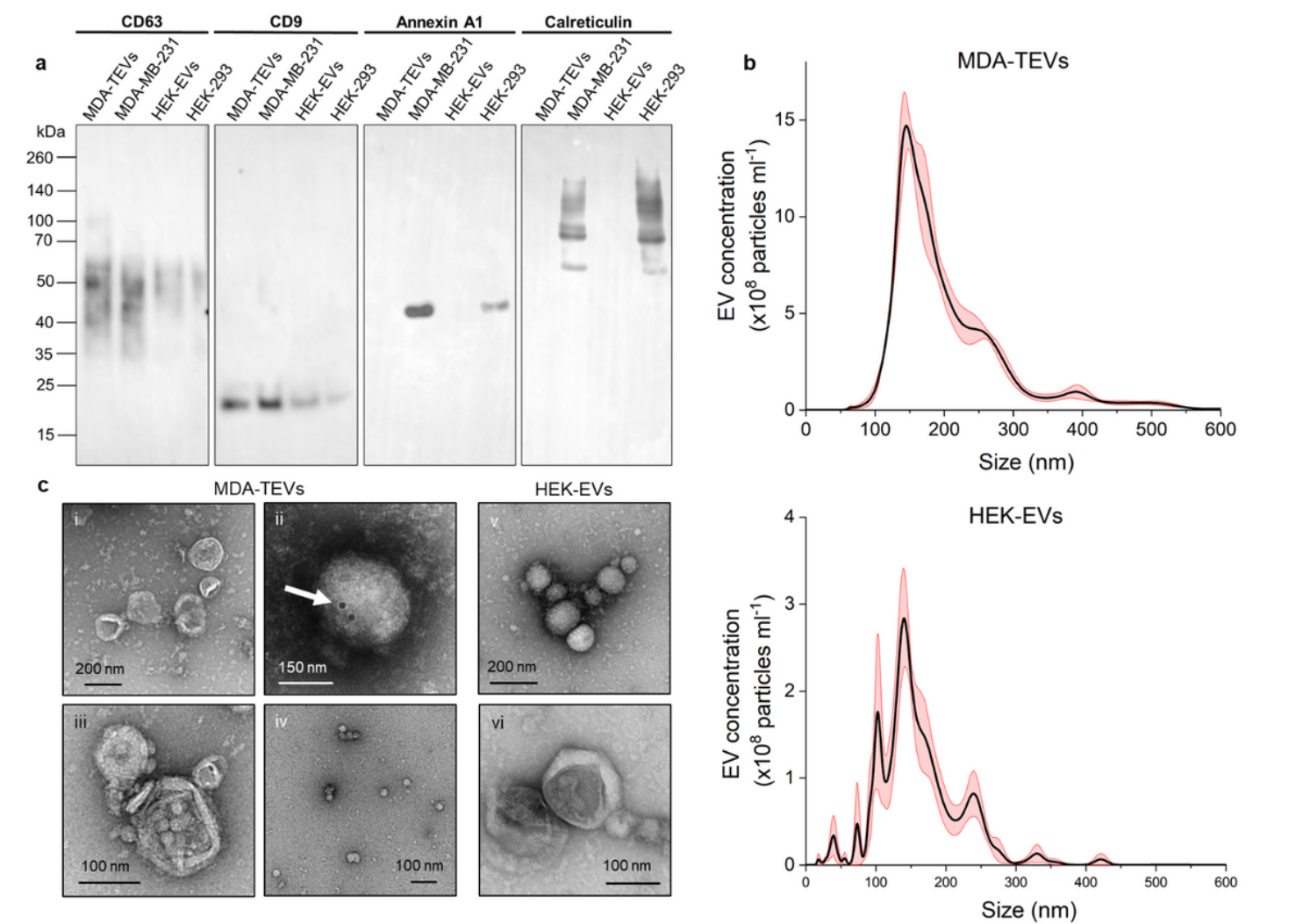


Figure 2

(a) Immunoblots of MDA-MB-231 and HEK-293 whole-cell lysates and (T)EV samples. Proteins were separated on SDS-PAGE gels and membranes were blotted with indicated antibodies. CD9, predicted: 25 kDa; CD63: smeared band between 35-60 kDa (multiple glycosylated forms influence gel migration,

therefore CD63 appears as a smear in the 30-60 kDa range, as expected⁶³.); annexin A1, predicted: 38 kDa; calreticulin, predicted: 55 kDa (other bands may indicate presence of dimers and multimers). Unedited immunoblots are available in the SI (**Fig. S1**). **(b)** Concentration (mean \pm s.e.m.; n=5 acquisitions from one sample per EV type) and size distribution, calculated by NTA, of EVs, with peak particle sizes of 153 ± 5.1 nm and 112 ± 12.7 nm for MDA-TEVs and HEK-EVs, respectively. **(c)** Representative negative stain TEM micrographs of indicated EVs (n=3 independent biological samples). **(c.i.)** MDA-TEVs. Scale bar, 200 nm. **(c.ii.)** MDA-TEV with 20 nm gold nanoparticles conjugated via CD63 antibody (white arrow). Scale bar, 150 nm. **(c.iii)** Close-up of MDA-TEV. Scale bar, 100 nm. **(c.iv)** Smaller MDA-TEVs. Scale bar, 100 nm. **(c.v)** HEK-EVs. Scale bar, 200 nm. **(c.vi)** Close-up of HEK-EV. Scale bar, 100 nm.

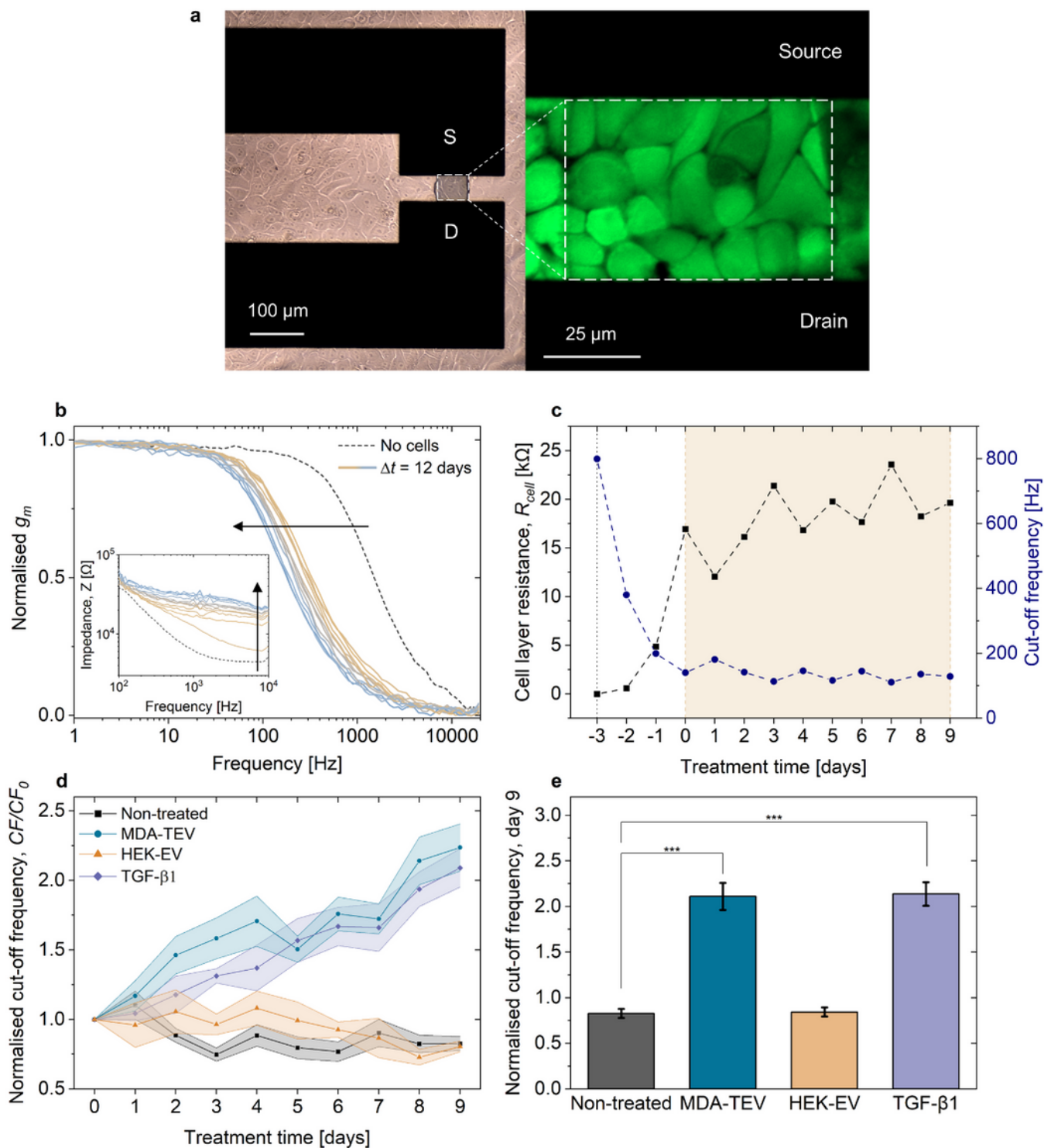


Figure 3

(a) Brightfield image of cells on the OECT device and zoomed in view of the channel with cells stained with viability/cytotoxicity kit probes (green-LIVE: calcein AM). The black boxes are the source and drain electrodes and the darkened area between them is the PEDOT:PSS channel. (b) Typical time evolution of the OECT frequency-dependent response as cells grow and form a confluent layer under normal culture conditions (non-treated). Inset graph shows the evolution of the impedance for non-treated cells. A

confluent layer of cells grown on the transistor channel induces a shift in the OECT cut-off frequency, from 860 Hz (dashed black line) to 140 Hz (solid blue line), and an increase in impedance from 4.9 k Ω to 26.4 k Ω . **(c)** Typical in-line monitoring of the cut-off frequency, as derived from the transconductance vs frequency plot, and the cell layer resistance (R_{cell}), as derived from the impedance vs frequency plot of non-treated cells. The vertical dotted line represents the baseline without cells on the device and the shaded area represents the treatment window. Equivalent representative cut-off frequency and R_{cell} plots are available for all conditions in **Fig. S3**. **(d)** Cut-off frequency normalised to day 0 (treatment start day) over time for the four experimental conditions: non-treated; 200 μ g MDA-TEVs; 185 μ g HEK-EVs; and 10 ng/ml TGF- β 1 (mean \pm s.e.m.; s.e.m. indicated by lightly coloured areas; n=3 and 2 for non-treated/MDA-TEV and HEK-EV/TGF- β 1, respectively). Data points before treatment day 0 are omitted for clarity. **(e)** Normalised cut-off frequency from treatment day 9 compared across the four conditions (mean \pm s.e.m). Two-way ANOVA. *** $p \leq 0.001$.

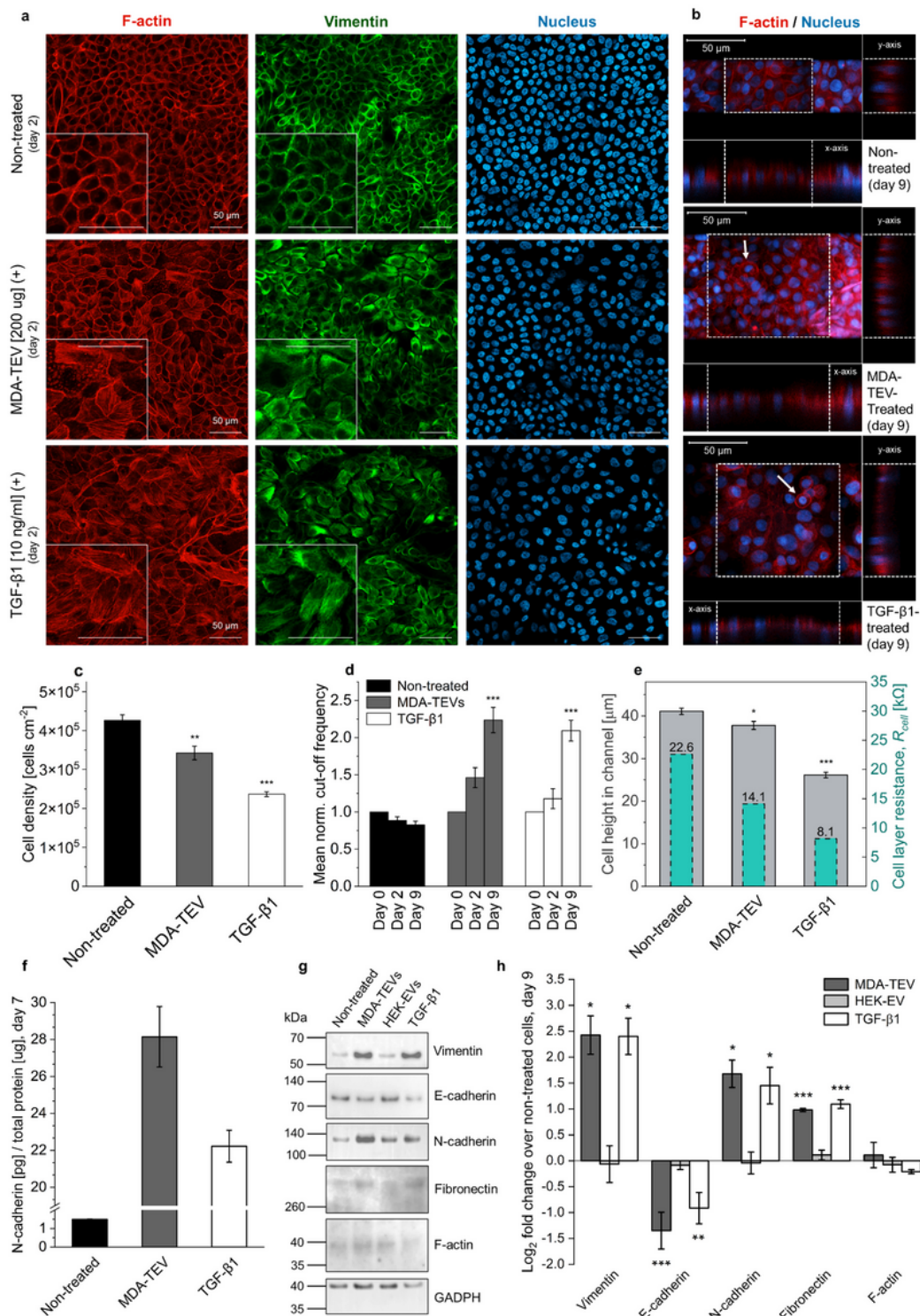


Figure 4

(a) Representative confocal images of immunofluorescently labelled MCF10A cells on treatment day 2; after 5 days of culture and 48 hours after addition of 200 μ g of MDA-TEVs and 10 ng/ml TGF- β 1, as indicated. Cells were stained for F-actin, vimentin, and nuclei. Insets show a close-up of cells. Scale bars, 50 μ m. (b) Representative x/z and y/z orthogonal views (ortho-views, right) of each cell layer in the OECT channel (treatment day 9), obtained by z-stacked confocal images. PEDOT:PSS channel is indicated by

white dotted lines. Cells were stained for F-actin and nuclei. Scale bars, 50 μm . White arrows indicate cells with a rounded morphology. **(c)** Cell density on treatment day 2 across conditions. Cell number was determined by counting cell nuclei from 5 frames (mean \pm s.e.m.). One-way ANOVA. **(d)** Normalised cut-off frequency from treatment day 0, 2, and 9 across conditions (mean \pm s.e.m.; n=3 and 2 for non-treated/MDA-TEV and TGF- β 1, respectively). Two-way ANOVA. **(e)** Cell height in channel derived from orthogonal projections (mean \pm s.e.m.; min. 8 measurements taken from different x- and y-positions; see **Fig. S7, Supplementary Videos 1-3**) and the cell layer resistance measured in each specific channel as derived from impedance (Z) plots. One-way ANOVA. **(f)** ELISA-based N-cadherin protein on treatment day 7 across conditions (mean \pm s.e.m.). One-way ANOVA. **(g)** Immunoblots of whole-cell lysates collected on treatment day 9. Equal quantities of protein were separated on SDS-PAGE gels and membranes were blotted with indicated antibodies. Vimentin, predicted: 54-75 kDa; E-cadherin, predicted: 97 kDa; N-cadherin, predicted: 125-135 kDa; fibronectin (slightly smeared due to glycosylation⁷⁸), predicted: 262-285 kDa; F-actin (slightly smeared), predicted: 42 kDa; and GADPH, predicted: 37 kDa. Unedited blots are available in **Fig. S8**. **(h)** Quantitative values of protein expression derived from immunoblots presented as Log₂ fold-change versus non-treated condition expression level (mean \pm s.e.m.; n=3). Two-way ANOVA. * $p \leq 0.05$, ** $p \leq 0.01$, *** $p \leq 0.001$.

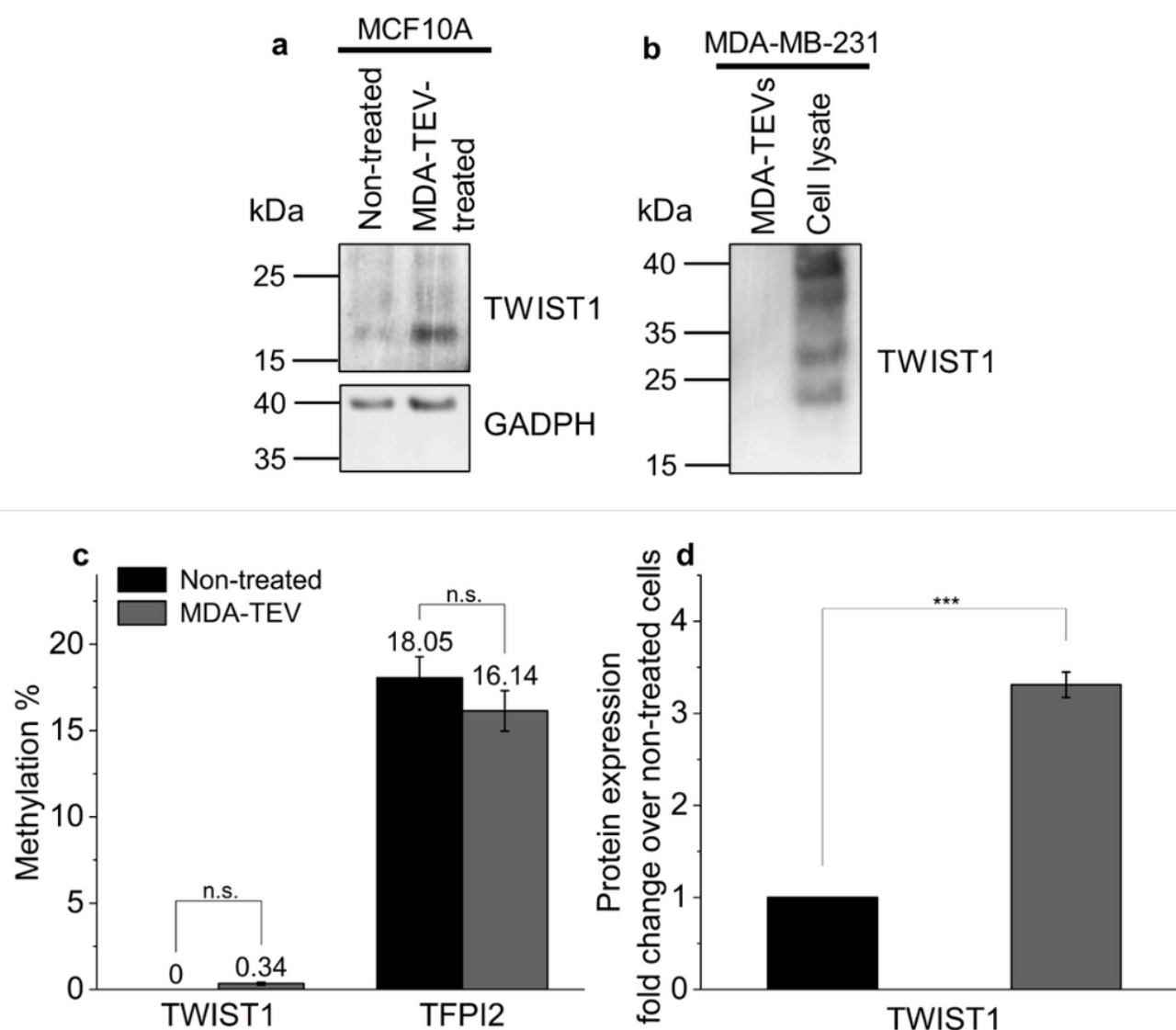


Figure 5

MDA-TEVs modulate TWIST1 protein expression but not DNA methylation level. **(a)** Immunoblots of whole-cell lysates collected on treatment day 9. **(b)** Immunoblot of MDA-TEVs and MDA-MB-231 whole-cell lysate. Equal quantities of protein were separated on SDS-PAGE gels and membranes were blotted with indicated antibodies. TWIST1, predicted: 21 kDa; GADPH, predicted: 37 kDa. Unedited blots are available in **Fig. S9**. **(c)** Total methylation (%) relative to house-keeping gene β -actin (mean \pm s.e.m.; $n=1$). **(d)** Quantitative values of protein expression derived from immunoblots presented as fold-change versus non-treated expression level (mean \pm s.e.m.; $n=3$). *** $p \leq 0.001$, n.s. = non-significant.

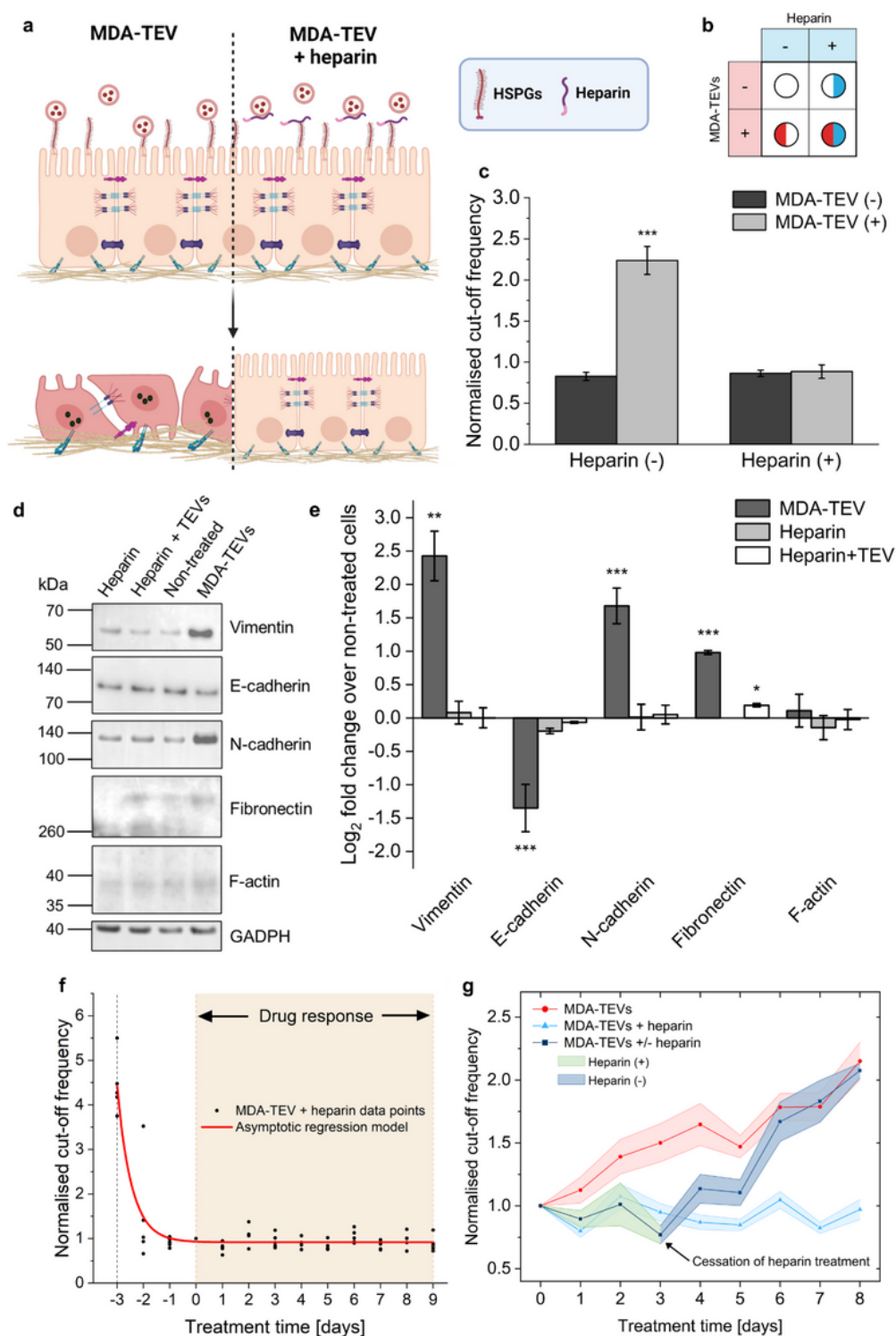


Figure 6

Heparin blocks MDA-TEV-induced EMT. **(a)** Schematic showing the proposed mechanism by which heparin binds to spike glycoproteins to out compete cell surface HSPGs and prevent EV adhesion and uptake. Created with Biorender.com **(b)** Two-factor factorial design to assess the effect of heparin treatment on MDA-EV-induced EMT. **(c)** Comparison of the normalised cut-off frequency on treatment day 9 between cells treated with MDA-TEVs in the absence (-) or presence (+) of heparin (mean \pm s.e.m.; $n=3$).

(d) Immunoblots of whole-cell lysates collected at the end of the experiment. Equal quantities of protein were separated on SDS-PAGE gels and membranes were blotted with indicated antibodies (same antibodies as listed in **Fig. 4**). Unedited immunoblots are available in **Fig. S8**. (e) Quantitative values of protein expression derived from immunoblots presented as Log_2 fold-change versus non-treated expression level (mean \pm s.e.m.; $n=3$). (f) Asymptotic regression model fitted to the drug response data points. (g) Heparin treatment temporarily blocks MDA-TEV-induced EMT. Cells were treated with heparin between day 0 and 3 (green coloured area) while exposed to MDA-TEVs. Washing cells with PBS to remove heparin and subsequently exposing cells to MDA-TEVs lead to an increase in cut-off frequency (dark blue coloured area). Data points before treatment day 0 are omitted for clarity (mean \pm s.e.m.; s.e.m. indicated by lightly coloured areas; $n=2$ and 3 for the transient heparin treatment condition (dark blue data points) and MDA-TEV (+/-) heparin (red and light blue data points), respectively. * $p \leq 0.05$, ** $p \leq 0.01$, *** $p \leq 0.001$.

Supplementary Files

This is a list of supplementary files associated with this preprint. Click to download.

- [TEVinducedEMTSIfinal.docx](#)
- [zstackvideoOECTTGFBeta1.avi](#)
- [zstackvideoOECTnontreated.avi](#)
- [zstackvideoOECTMDATEV.avi](#)